

Calculating the Band Structure of Photonic Crystals

Project Code: PHOT-McCall-1

CID: 00828489

Supervisor: Martin McCall

Assessor: Mike Damzen

Word Count: 9148

02/04/2018

Abstract

Two methods for calculating the band structures of photonic crystals were implemented in MATLAB utilising the truncated Fourier expansion of the source-less Maxwell's equations in the case of non-magnetic and magnetic unit cells respectively. Both methods were found to be convergent and to have good agreement with existing literature. A novel technique for finding the Fourier coefficients for non-rectangular arrays using the standard Fast Fourier Transform (FFT) is utilised to calculate the band structure for near-arbitrary unit cells, from the use of non-primitive unit cells.

Contents:

1.	Introduction.....	4
2.	Theory: The Plane Wave Expansion Method.....	5
3.	Semi-Analytic Non-Magnetic Implementation.....	9
4.	Semi-Analytic Non-Magnetic Results.....	11
5.	Rumpf Implementation.....	17
6.	Rumpf Results.....	20
7.	Non-Primitive Unit Cells.....	28
8.	Conclusions.....	36
9.	Acknowledgements.....	37
10.	Bibliography.....	37

Appendices

A.	Derivation of Semi-Analytic Non-Magnetic Method Equation.....	38
B.	Derivation of 1D Box Function Fourier Series.....	40
C.	Derivation of 2D Circular Rod Fourier Series.....	41
D.	Hexagonal Fast Fourier Transform (HFFT).....	43

1. Introduction

A Photonic Crystal is a periodic material whose electric permittivity, ϵ , and magnetic permeability, μ , are spatially variable. As such they can be described by the tiling of a ‘unit cell’ over a Bravais lattice. These can occur naturally, for example Precious Opal is composed of a regular packing of silica spheres, in addition to being constructed artificially. One dimensional photonic crystals, where the crystal is uniform in two directions have been studied for over a century under various guises [1], but the modern name of ‘photonic crystals’, and the application of solid state electronic band structure techniques came courtesy of E. Yablonovitch in 1987 [2,3].

While 1D photonic crystals have existed for a long time, and can now be manufactured on a very small scale using techniques such as chemical vapour deposition [4], the creation of 2D and 3D crystals is still limited by fabrication techniques, especially for more elaborate unit cell geometries. As such, computational methods to determine the band structures of photonic crystals are necessary.

Bloch’s theorem shows that light propagating through the periodic medium of a photonic crystal will have its magnetic and electric field components composed of a periodic spatial function, $\varphi(\mathbf{r})$, and a plane wave characterised by a Bloch crystal wave vector, β .

For any given β , there are many corresponding physically possible φ s, each with a different frequency, ω , dividing the possible propagating light waves into discrete bands. For light shone on a photonic crystal, it is its frequency, ω_i , which is preserved within the crystal – the light can couple to any β with a matching frequency mode, $\omega = \omega_i$. However, if the incident frequency falls in a ‘band gap’ – a range of frequencies where there are no corresponding crystal wave vectors – then the light cannot propagate within the crystal and is perfectly reflected (see Figure 1).

A very useful property of photonic crystals is that their band structure is inversely proportional to the size of the unit cell. This means a feature in a crystal’s band structure – a band gap for example – can be tuned to any frequency of light by resizing the unit cell of the crystal appropriately. Because of this, frequencies in band structures are expressed as ‘Normalised Frequencies’, $\omega a / 2\pi c$, where a is the length scale of the unit cell. Similarly, band gaps are often expressed as the ‘gap-midgap ratio’, $\Delta\omega / \omega_m$, the ratio between the size of the

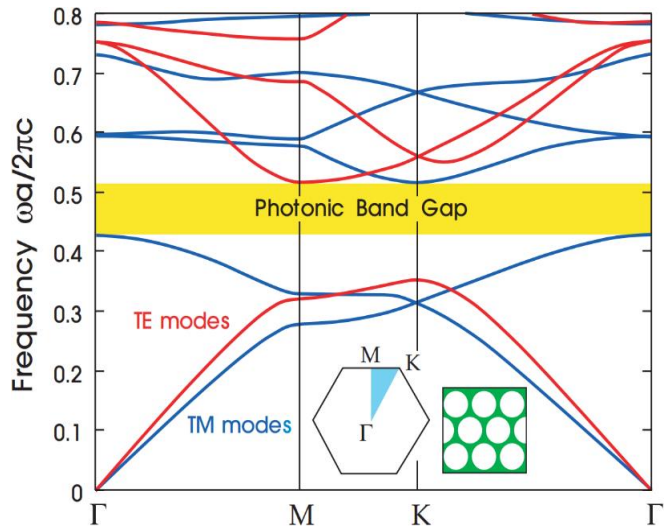


Figure 1: This shows an example of a band structure with a band gap, with unit cell geometry and reciprocal space trace within the 1st Brillouin Zone (BZ). Image from “Photonic Crystals: Molding the Flow of Light” J. Joannopoulos [5, p76].

band gap and the normalised frequency in the middle of the band gap. This is also invariant to scaling of the unit cell.

These band gaps already have industrial applications as they can be used to create waveguides by introducing a ‘defect’, a unit cell or series of unit cells which have different permittivity and/or permeability from the rest of the crystal. For example, Figure 2 shows a prototype photonic crystal fibre for optical communication, where the central unit cell has a defect. Light shone into this defect at a band gap frequency for the rest of the crystal will remain bound to the central unit cell defect, but free to travel along it in the third dimension. These photonic crystal fibres theoretically have much better attenuation properties than conventional total internal reflection optical fibres [7].

The primary objective of this project was to develop MATLAB code able to calculate the photonic band structure of photonic crystals with simple geometries and isotropic materials. While photonic crystals can be 1, 2 or 3 dimensional and the methods described here are equally applicable to all dimensionalities, only 1D and 2D crystals are explored in this project.

2. Theory: The Plane Wave Expansion Method

Taking the source-less Maxwell’s Equations as a starting point (1), the two curl equations can be re-expressed in the frequency domain (2). Thus, by eliminating the electric field, \underline{E} , the magnetic field can be given by a second order differential equation (3).

$$\nabla \cdot \underline{B} = 0, \quad \nabla \cdot \underline{D} = 0, \quad \nabla \times \underline{E} = -\frac{\partial \underline{B}}{\partial t}, \quad \nabla \times \underline{H} = \frac{\partial \underline{D}}{\partial t} \quad (1)$$

$$\nabla \times \underline{E} = -i\omega \underline{B} = -i\omega \mu \underline{H}, \quad \nabla \times \underline{H} = i\omega \underline{D} = i\omega \epsilon \underline{E} \quad (2)$$

$$\nabla \times \left(\frac{1}{\epsilon} \nabla \times \underline{H} \right) = \omega^2 \mu \underline{H} \quad (3)$$

Expanding $\epsilon(\underline{r}) = \epsilon_0 \epsilon_r(\underline{r})$ and $\mu(\underline{r}) = \mu_0 \mu_r(\underline{r})$, this becomes:

$$\nabla \times \left(\frac{1}{\epsilon_r} \nabla \times \underline{H} \right) = \omega^2 \epsilon_0 \mu_0 \mu_r \underline{H} = \frac{\omega^2}{c^2} \mu_r \underline{H} = k_0^2 \mu_r \underline{H} \quad (4)$$

In the limit of an infinite photonic crystal, the Fourier transform of the crystal's permittivity and permeability is equivalent to the Fourier series for the unit cell itself. Every field in the above equations can be expanded as a series of plane waves, $e^{i(\underline{k}\cdot\underline{r}-\omega t)}$, or since every term will have the same ω dependence, $e^{i\underline{k}\cdot\underline{r}}$.

$$\frac{1}{\varepsilon_r(\underline{r})} = \sum_{\underline{G}} K(\underline{G}) e^{i\underline{G}\cdot\underline{r}}, \quad \varepsilon_r(\underline{r}) = \sum_{\underline{G}} a(\underline{G}) e^{i\underline{G}\cdot\underline{r}}, \quad \mu_r(\underline{r}) = \sum_{\underline{G}} b(\underline{G}) e^{i\underline{G}\cdot\underline{r}} \quad (5)$$

$$\underline{H}(\underline{r}) = \underline{h}_{\beta}(\underline{r}) e^{i\underline{\beta}\cdot\underline{r}} = \sum_{\underline{G}} (\underline{h}_{\beta}(\underline{G}) e^{i\underline{G}\cdot\underline{r}}) e^{i\underline{\beta}\cdot\underline{r}} \quad (6)$$

$$\underline{E}(\underline{r}) = \underline{e}_{\beta}(\underline{r}) e^{i\underline{\beta}\cdot\underline{r}} = \sum_{\underline{G}} (\underline{e}_{\beta}(\underline{G}) e^{i\underline{G}\cdot\underline{r}}) e^{i\underline{\beta}\cdot\underline{r}}, \quad (7)$$

where \underline{G} are integer sums of the reciprocal lattice vectors, $p\underline{b}_1$ for 1D, and $p\underline{b}_1 + q\underline{b}_2$ for 2D crystals

$$\underline{b}_1 = 2\pi \frac{\underline{a}_2 \times \underline{a}_3}{\underline{a}_1 \cdot (\underline{a}_2 \times \underline{a}_3)}, \quad \underline{b}_2 = 2\pi \frac{\underline{a}_3 \times \underline{a}_1}{\underline{a}_1 \cdot (\underline{a}_2 \times \underline{a}_3)}, \quad (8)$$

where \underline{a}_1 , \underline{a}_2 and \underline{a}_3 are the lattice vectors themselves. Given 3D crystal lattices are not being worked with, \underline{a}_3 can always be taken to be a unit vector orthogonal to \underline{a}_1 and \underline{a}_2 (and similarly for \underline{a}_2 in a 1D crystal). The reciprocal lattice vectors define the 1st Brillouin Zone (BZ).

As plane waves with different wave vectors, \underline{k} , are orthogonal, the wave vectors on the left- and right-hand sides of the equations must be equal, splitting Maxwell's equations into an infinite series of dependent equations. However, most unit cell geometries can be well approximated by a truncated Fourier series, with only a finite number of Fourier components (harmonics). This finite set of dependent equations can then be expressed as an eigenvalue problem and solved computationally – the Plane Wave Expansion Method.

This method is applicable to both 1D and 2D crystals, though for 2D crystals the truncated Fourier series itself will be 2D, and hence can be truncated to a different number of harmonics, P and Q, in each dimension. In this report, assume that P = Q for any calculation, unless otherwise specified, i.e. there will be P plane waves in the truncated Fourier series for a 1D crystal, and P² plane waves for a 2D crystal.

Additionally, for 2D crystals the polarisation of the light wave must be considered. As the crystal is uniform in the third dimension, there is no need to consider any wave vector components orthogonal to plane of the crystal – the wave vector can be assumed to be in the plane. Therefore, incident light of any polarisation orientation can be expressed as a superposition of two light waves with the electric and magnetic field orthogonal to the plane of the crystal – 'Transverse Electric' (TE) and 'Transverse Magnetic' (TM) modes respectively. These orthogonal modes interact with the crystal differently, yielding different band structures.

The band structure itself can be calculated by building the eigenproblem for a range of different Bloch crystal wave vectors, β . Solving each of them gives the range of frequencies which can propagate with that wave vector, and so interpolating between β s produces the band structure (see Figure 3).

Strictly speaking, the normalised frequencies should not simply be joined in ascending order as bands can cross – with a simple ascending order method, crossing bands will appear to ‘bounce’ off each other. Instead the frequencies should be sorted according to which periodic spatial function, φ , best matches each φ' for an adjacent β . In practice however, this is an unnecessary level of precision. When looking for band gaps, it doesn’t matter what the magnetic field looks like, only whether a mode exists at a given frequency. In principle the ‘bounce’ could predict a tiny band gap which does not physically exist, but in practice this is almost never observed.

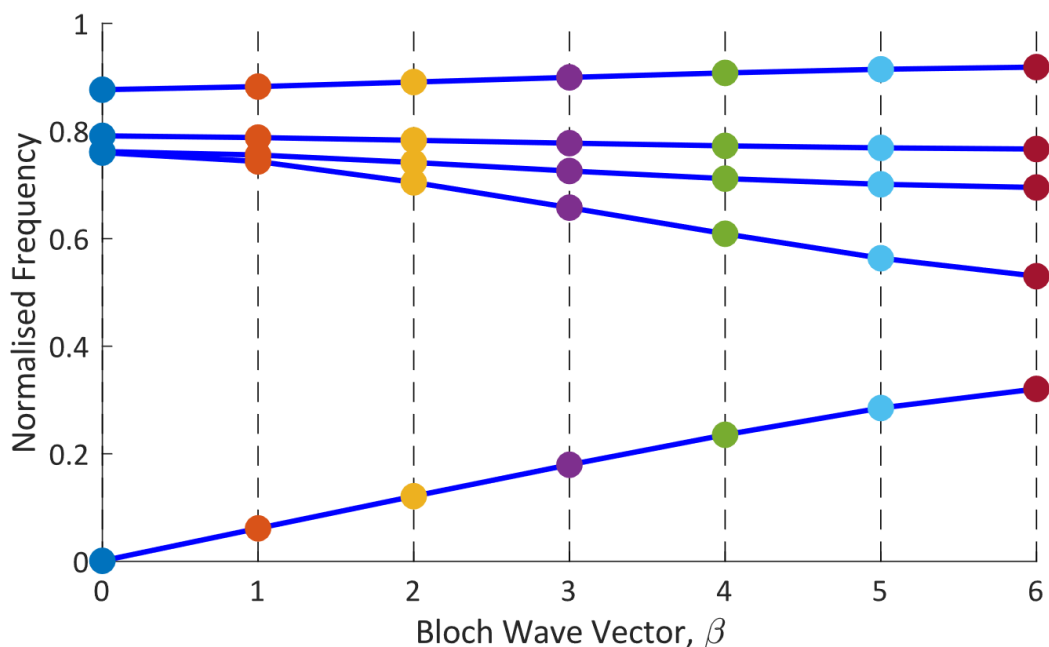


Figure 3: This figure shows the first 5 TE eigenvalues for 7 β s stepping a small distance away from the centre of the 1st BZ. For each β , the eigenvalues are calculated, converted to normalised frequency and then plotted, giving the coloured dots for each β above. Then, the points are interpolated between in ascending order to estimate the band structure – the blue lines.

For 1D crystals, the range of β s will be the full 1st Brillouin zone (BZ), but for 2D crystals, it is usually only worth calculating the band structure for β s on the perimeter of the irreducible Brillouin zone (IBZ) – the part of the 1st BZ that remains once unit cell symmetries have been removed (see Figure 4). This is because band extrema almost always occur here, and band extrema are all that matter when finding band gaps [5, p68]. Intuitively, this is due to

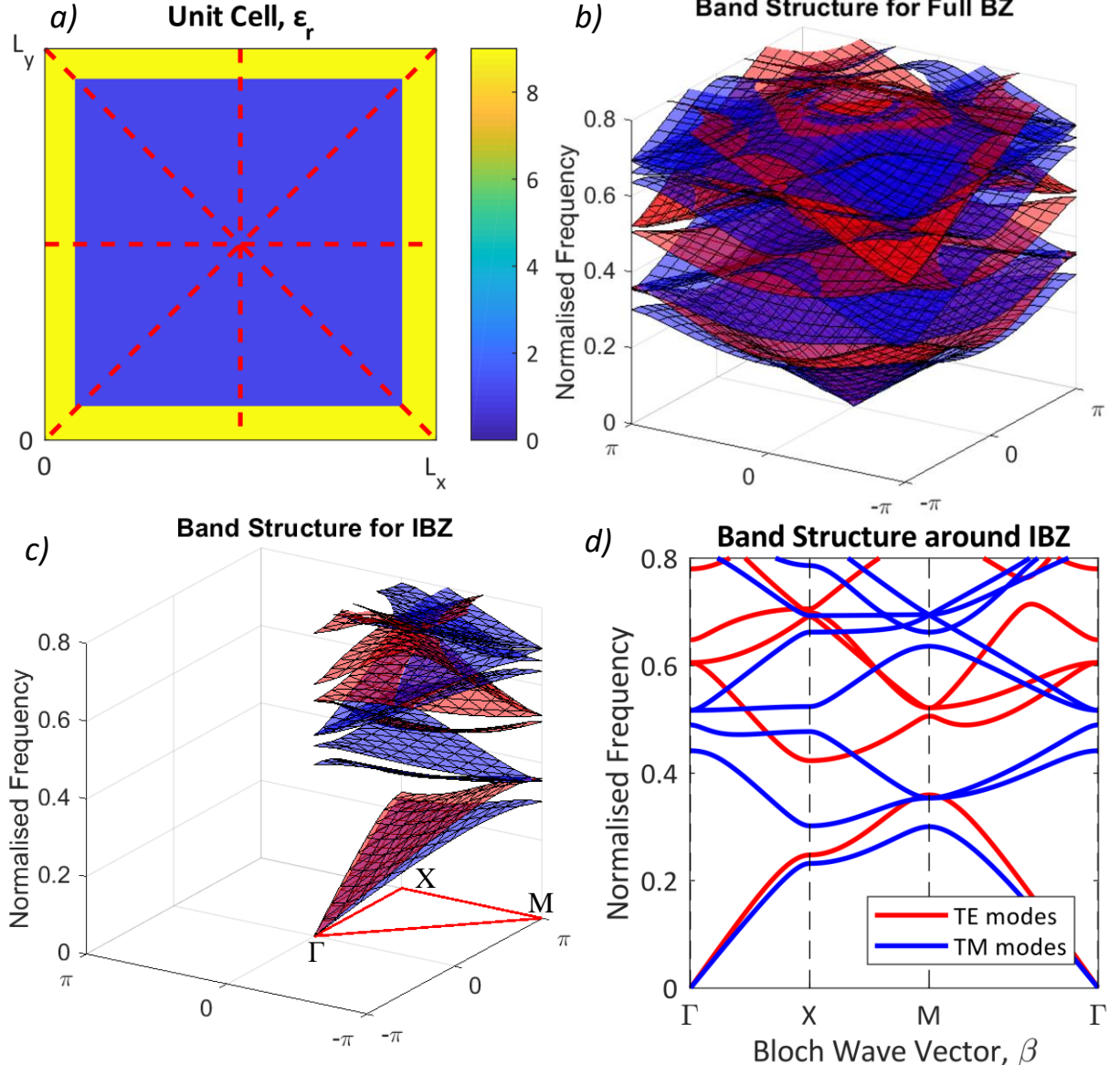


Figure 4: These diagrams show how the conventional plotting of band structures for photonic crystals relate to the 1st BZ of a crystal. In a) the relative permittivity of the unit cell used to calculate the band structure is shown – a dielectric ($\epsilon_r = 8.9$) with square holes of air ($\epsilon_r = 1$) drilled into it. The red lines superimposed over it show the symmetries of the unit cell, and for its 1st BZ. In b), a 3d plot shows an estimation of the complete band structure over the 1st BZ, with the BZ estimated by a 21x21 grid of Bloch wave vectors, β . Eliminating the symmetries shown in a) from this yields the reduced band structure shown in c) across the IBZ. It also shows the labels given to the key points around the IBZ, Γ , X and M. Finally, d) shows the band structure around perimeter of the IBZ, with 200 β s equally spaced between each key point. All three band structures are calculated with 7 harmonics in both directions, giving 49 plane waves in total using the Rumpf method (Sections 5,6).

symmetry arguments – on the edges of the IBZ, the partial derivative of the band surface orthogonal to the IBZ edge must be zero. So for band extrema to appear on the edge of the IBZ, only one more partial derivative needs to be zero – much more likely to happen than for two to appear in the same place elsewhere in the IBZ.

There are many different methods of building a computationally solvable eigenproblem from Maxwell's equations, but in this report only two will be discussed.

3. Semi-Analytic Non-Magnetic Implementation

For the first of these methods, the first step was to simplify the problem by assuming the relative magnetic permeability of the unit cell, μ_r , has a constant value of 1, i.e. non-magnetic. This is a fair approximation for conventional materials, which rarely have significant relative magnetic permeability. Further, it was assumed that the Fourier components of the unit cell could be calculated analytically. This allows the band structure to be calculated for any Bravais lattice. In contrast, the Fast Fourier Transform (FFT) is only applicable to rectangular unit cells. However, realistically this assumption instead limits the method to working with simple unit cell geometries only. Finally, a truncated Fourier series was used – the first P, or P^2 harmonics for 1D and 2D crystals respectively – i.e. semi-analytic.

Substituting the Fourier expansions of the unit cell into Equation (4) yields:

$$\nabla \times \left(\sum_{\underline{G}} K(\underline{\tilde{G}}) e^{i\underline{\tilde{G}} \cdot \underline{r}} \nabla \times \sum_{\underline{G}} (\underline{h}_{\beta}(\underline{G}) e^{i\underline{G} \cdot \underline{r}}) e^{i\underline{\beta} \cdot \underline{r}} \right) = k_0^{-2} \sum_{\underline{G}} (\underline{h}_{\beta}(\underline{G}) e^{i\underline{G} \cdot \underline{r}}) e^{i\underline{\beta} \cdot \underline{r}} \quad (9)$$

From which it can be shown by mode matching and expanding the curl terms (see Appendix A):

$$-\sum_{\underline{G}} K(\underline{G}' - \underline{G}) (\underline{G}' + \underline{\beta}) \times ((\underline{G} + \underline{\beta}) \times \underline{h}_{\beta}(\underline{G})) = k_0^{-2} \underline{h}_{\beta}(\underline{G}') \quad (10)$$

For a 1D crystal, \underline{G} , \underline{G}' and $\underline{\beta}$ all lie parallel to the crystal variation, and \underline{h} orthogonal to it. This therefore simplifies to:

$$-\sum_{\underline{G}} K(\underline{G}' - \underline{G}) |\underline{G}' + \underline{\beta}| |\underline{G} + \underline{\beta}| \underline{h}_{\beta}(\underline{G}) = k_0^{-2} \underline{h}_{\beta}(\underline{G}') \quad (11)$$

For 2D crystals, \underline{G} , \underline{G}' and $\underline{\beta}$ all lie in the plane of the crystal variation, and \underline{h} has some component in the plane, and some component orthogonal to it. Let $(\underline{G} + \underline{\beta})$ and $(\underline{G}' + \underline{\beta})$ be parallel to unit vectors \underline{v}_3 and \underline{v}_3' respectively, and orthogonal to vectors \underline{v}_1 , \underline{v}_2 and \underline{v}_1' , \underline{v}_2' respectively, as per Figure 5. Both sets of vectors form an orthonormal coordinate system

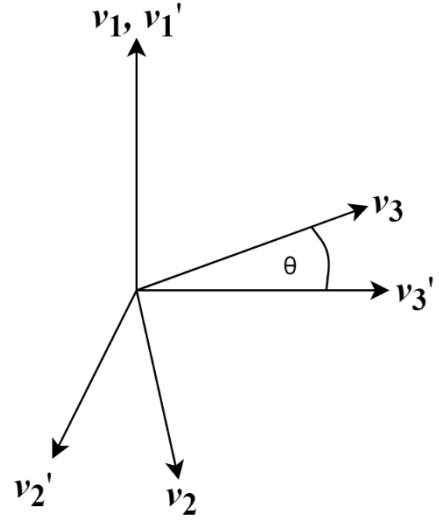


Figure 5: this diagram shows the relative directions of \underline{v}_1 – \underline{v}_3 and $\underline{v}_1' - \underline{v}_3'$.

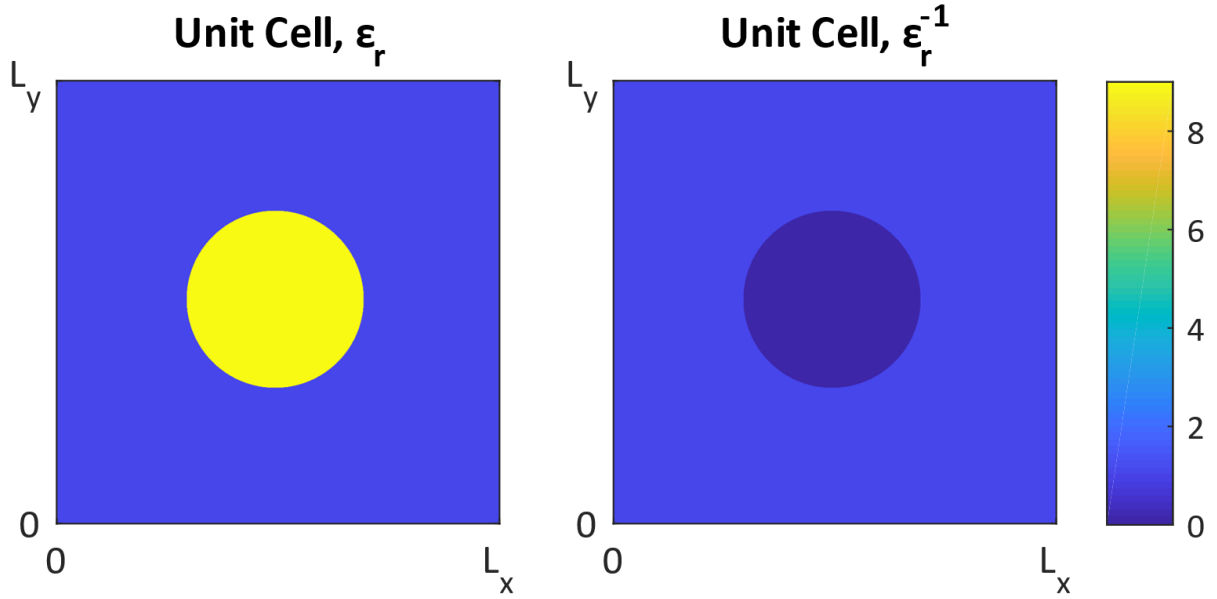


Figure 6: These plots show how in a unit cell with discrete values for permittivity, the unit cell and reciprocal of the unit cell have discontinuities in the same places. This means the form of the respective Fourier series will be very similar (see Appendix C). In this diagram a circular column of dielectric, with $\epsilon_r = 8.9$ is surrounded placed within a square unit cell of air, $\epsilon_r = 1$.

allowing easy calculation of the cross-product. Using this, the cross products can be calculated by expanding \underline{h} in these bases:

$$\underline{h} = h_1 \underline{v}_1 + h_2 \underline{v}_2 + h_3 \underline{v}_3 = h'_1 \underline{v}_1' + h'_2 \underline{v}_2' + h'_3 \underline{v}_3' \quad (12)$$

$$(\underline{G}' + \underline{\beta}) \times ((\underline{G} + \underline{\beta}) \times \underline{h}) = - |\underline{G}' + \underline{\beta}| |\underline{G} + \underline{\beta}| (h_1 \cos \theta \underline{v}_1' + h_2 \underline{v}_2') , \quad (13)$$

where θ is the angle between vectors \underline{v}_3 and \underline{v}_3' . Thus, the full problem becomes:

$$\sum_{\underline{G}} K(\underline{G}' - \underline{G}) |\underline{G}' + \underline{\beta}| |\underline{G} + \underline{\beta}| \begin{pmatrix} \cos \theta & 0 \\ 0 & 1 \end{pmatrix} \begin{pmatrix} h_{\underline{\beta}1}(\underline{G}) \\ h_{\underline{\beta}2}(\underline{G}) \end{pmatrix} = k_0^2 \begin{pmatrix} h'_{\underline{\beta}1}(\underline{G}') \\ h'_{\underline{\beta}2}(\underline{G}') \end{pmatrix} \quad (14)$$

This is essentially two eigenproblems of the form, $A\underline{v} = \lambda \underline{v}$, which can be solved using standard computational methods – in this case the MATLAB ‘eig’ function – one for the TE modes, and one for the TM. Algebraically, this method is similar to that used by M. Plihal in “Two-dimensional photonic band structures”, 1991 [8]. The eig function returns a list of eigenvalues, k_0^2 , which can be put in the form of the normalised frequency, $\omega a / 2\pi c$, by:

$$\frac{\omega a}{2\pi c} = \frac{a}{2\pi} \sqrt{k_0^2} \quad (15)$$

Note that the relative permittivity of the unit cell is now expressed as the Fourier series of its reciprocal, K . Therefore a 3 component Fourier series from a sinusoidal variation in permittivity, ϵ_r , becomes a messy infinite Fourier series in K . However, most real-world photonic crystals currently use just two materials with discrete permittivities, rather than blends with continuous permittivities, so the form of K is actually fairly similar to ϵ_r , only with a different pair of values to step between (see Figure 6).

Note also that $K(\underline{\mathbf{G}}' - \underline{\mathbf{G}})$ is effectively a convolution matrix for $K(\underline{\mathbf{G}})$, i.e.

$$K(\underline{\mathbf{G}}') * A(\underline{\mathbf{G}}) = K(\underline{\mathbf{G}}' - \underline{\mathbf{G}})A(\underline{\mathbf{G}}), \quad (16)$$

where $A(\underline{\mathbf{G}})$ is some field in reciprocal space.

Initially, this eigenproblem was constructed element by element using ‘for’ loops to calculate each entry in the eigenproblem matrix independently for each $\underline{\mathbf{G}}$ and $\underline{\mathbf{G}'}$, essentially requiring the same piece of code to be run P^4 times for each β . This was greatly improved by eliminating the four harmonic loops, and utilising MATLAB’s efficient matrix operations instead, giving an approximate factor of 3 reduction in runtime. This was then also improved upon by using parallel processing to solve the eigenproblem for multiple β s simultaneously – MATLAB’s ‘parfor’ parallelised for loop. This reduced runtime by an additional 30%.

In principle, an iterative method for finding eigenvalues should be highly effective here, as neighbouring β s have similar eigenvectors. The solution for one β would make a very good 1st estimate for the solution to the next, allowing an iterative method to rapidly find the eigenvectors for the full set of β s. In practice however, all attempted implementations for this were far slower than MATLAB’s ‘eig’ function, and so this idea was not used.

4. Semi-Analytic Non-Magnetic Results

Having implemented this computational method, the question becomes whether it is an accurate calculator. There are two key questions about the calculated band structure that need to be resolved for this – does it converge as the number of harmonics used is increased, and does it match with the existing literature for a given crystal unit cell?

First, consider a 1D crystal with a simple box function describing the permittivity of the unit cell (see Figure 7). The analytic expression for the Fourier series for such a unit cell is given by the sinc function, $\text{sinc}(x) = \frac{\sin(x)}{x}$ (see Appendix B). This was implemented in the code, and the band structure calculated for a range of harmonics, P , as shown in Figure 8.

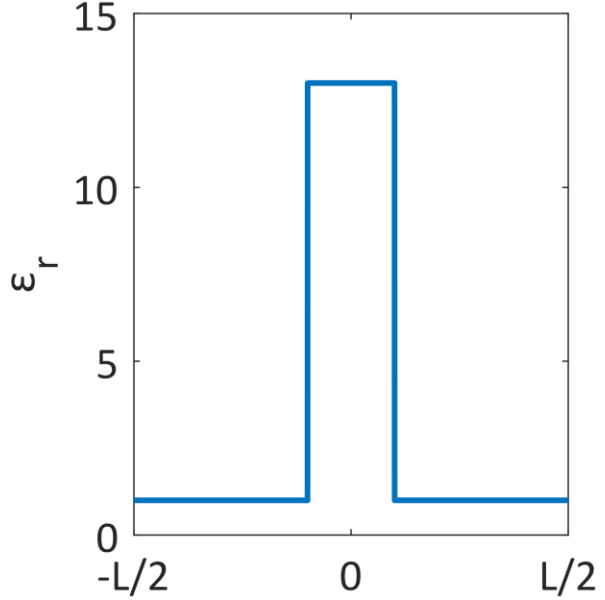


Figure 7: This graph shows the relative permittivity, ϵ_r , of a 1D photonic crystal unit cell. This corresponds to a thin slab of dielectric ($\epsilon_r = 13$, width = $0.2L$) in air ($\epsilon_r = 1$).

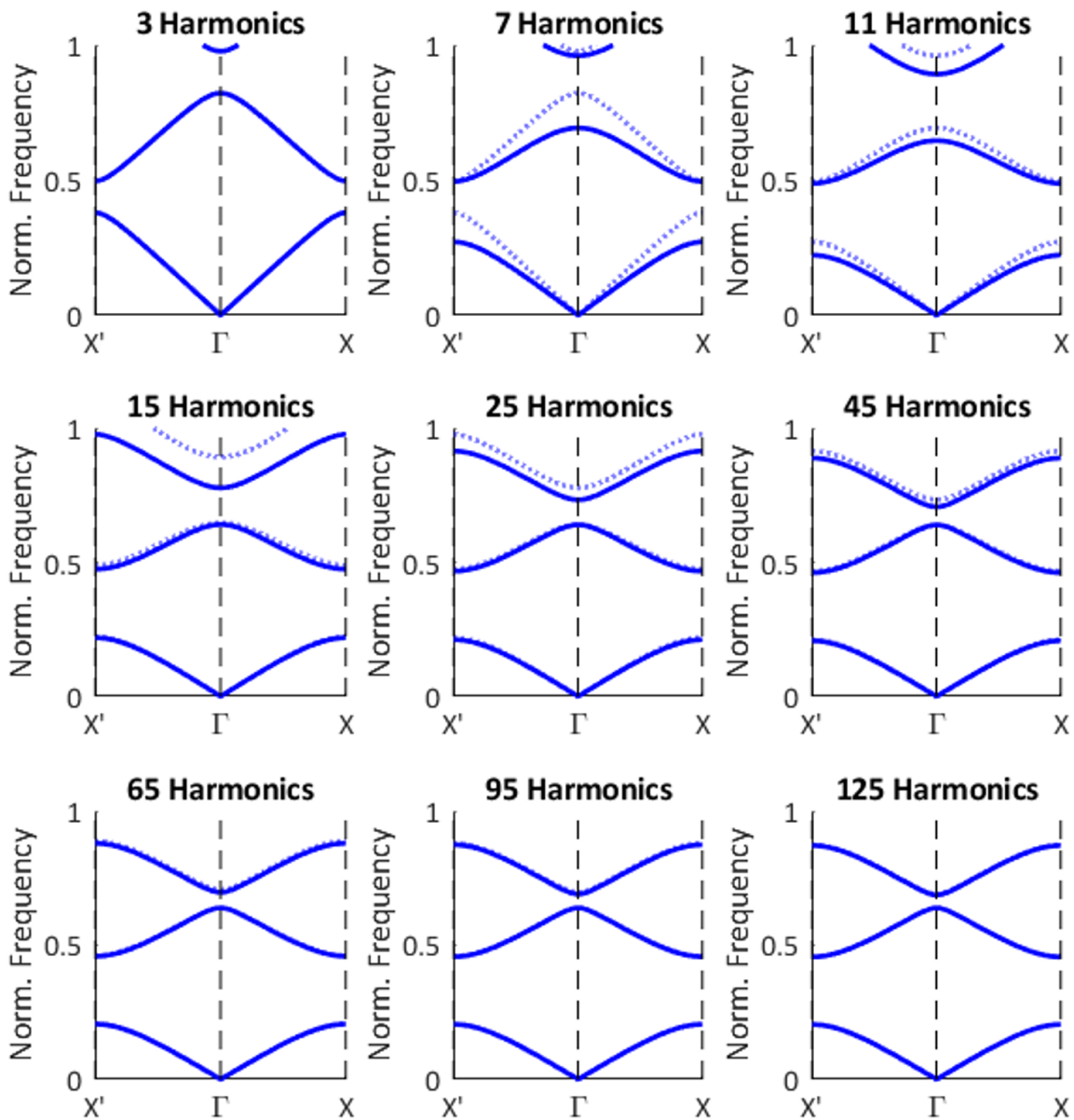


Figure 8: This figure shows the calculated band structure for a 1D photonic crystal with a unit cell as given in Figure 7, for a range of harmonics from 3 to 125. Each graph shows the band structure from the previous graph as a dotted line, to help show how the band structure changes as the harmonics increase. At 125 harmonics, $\Delta\omega/\omega_m = 0.7620$ for the first band gap.

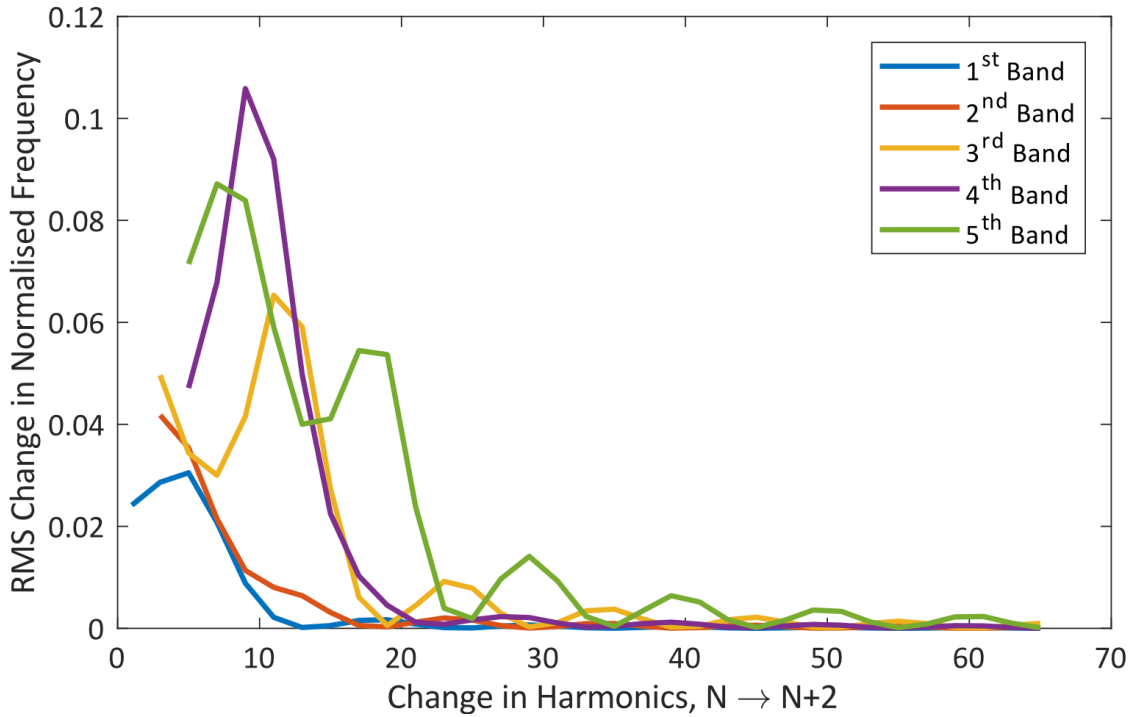


Figure 9: This graph shows the average change in normalised frequency across all points in each of the first 5 bands, as the number of harmonics used to calculate the band structure is increased. The RMS is used as it effectively measures the overall agreement between the two versions of the band.

Thus, it is clear the band structure does indeed converge. In fact, plotting the average squared differences in the first 5 bands between consecutive Ps yields the graph shown in Figure 9 – clearly convergent, showing that as the number of harmonics increases the change in the bands tends to zero. It also shows that lower frequency bands converge faster than high frequency bands.

Physically this is because the unit cell is only being simulated using a truncated Fourier series, and so Gibb's phenomenon is seen around the discontinuities in ε_r (see Figure 10). As the number of harmonics is increased, the width of the Gibb's overshoot decreases, reducing the sensitivity of the low frequency (long wavelength) bands to the overshoots. Conversely, as the frequency of the band increases, the accuracy of the calculation deteriorates due to this effect.

Comparing the calculated band structure to literature values for this unit cell, strong agreement is found between the 125 harmonics calculation and the band structure for the same crystal given by J. Joannopoulos in

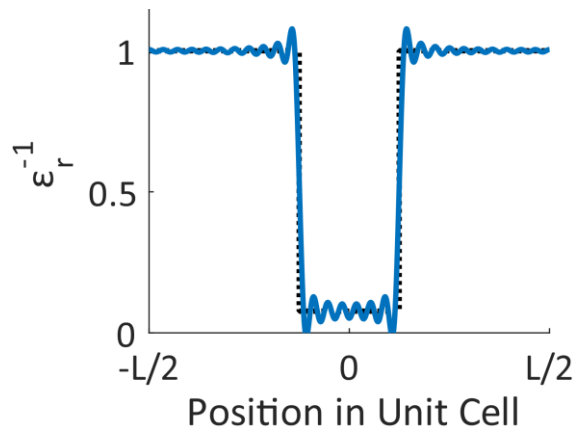


Figure 10: This graph shows a 55 harmonic approximation to the box function unit cell shown in Figure 7. Note the Gibb's overshoot of ~0.1 on both sides of the discontinuities.

"Photonic Crystals: Molding the Flow of Light" [5, p51]. He calculates a gap-midgap ratio for the first band gap of 0.763, almost identical to the 0.762 value found with this method at 125 harmonics.

Therefore, it is reasonable to say the calculator works well for this crystal cell. Testing other 1D geometries yields similar results.

Moving on now to 2D crystals, the Fourier coefficients for a unit cell with a circular feature (see Figure 11) can be described using a Bessel function, as shown in Appendix C. Thus, the Fourier coefficients for a square array of circular dielectric columns in air can be calculated analytically.

Plugging this into the calculator, the band structure is shown to converge as the number of harmonics increases (see Figure 12). Once again, when a large number of harmonics are used for the calculation, the result is found to have strong agreement with the band structure calculated by J. Joannopoulos [5, p68]. Note his band structure shows only the lowest four TE and TM bands, so does not show the start of the fifth TM mode around X .

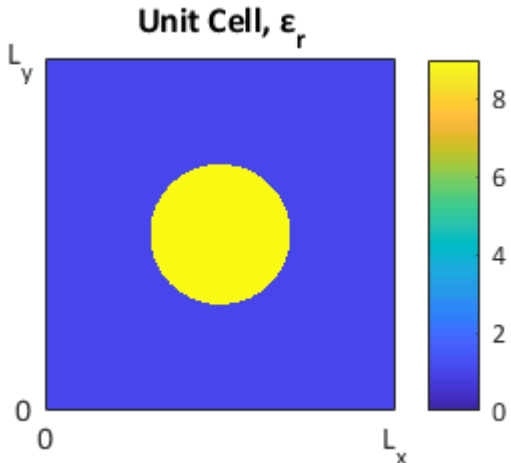


Figure 11: This image shows the relative permittivity, ϵ_r , of an example 2D photonic crystal unit cell. This corresponds to a circular column of dielectric ($\epsilon_r = 8.9$, $r = 0.2L_x$) in air ($\epsilon_r = 1$).

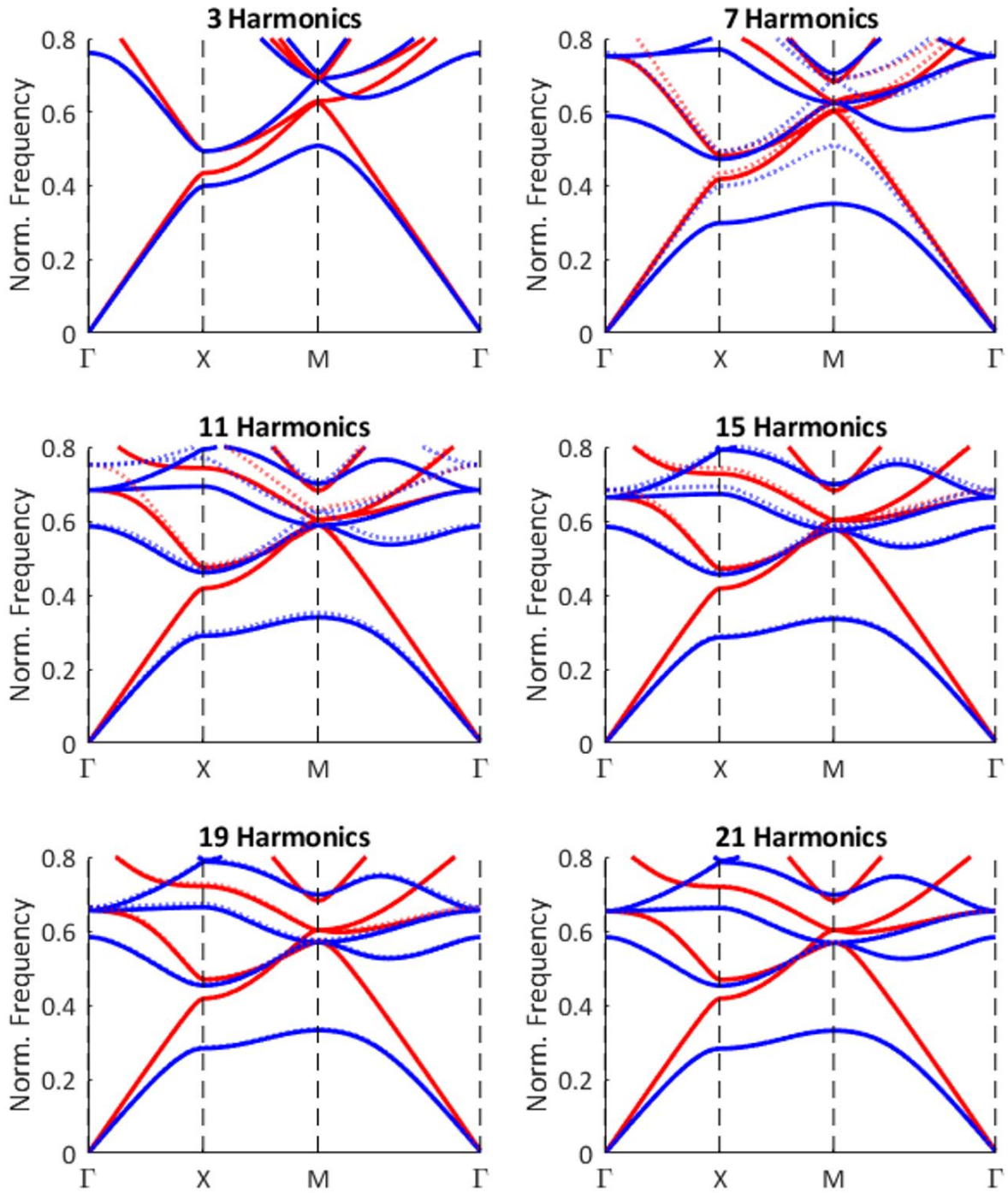


Figure 12: This figure shows the calculated band structure for a 2D photonic crystal with a unit cell as given in Figure 11, for a range of harmonics from 3 to 21, i.e. 9 to 441 plane waves. Each graph shows the band structure from the previous graph as a dotted line, to help show how the band structure changes as the harmonics increase. Note there is almost no change in the band structure from 15 to 21 harmonics – the band structure converges. Blue and red lines denote TM and TE modes respectively.

To show the circular feature is not the only type of feature the calculator can work with, consider an infinite crystal of dielectric with a square pattern of square air holes drilled into it, i.e. the unit cell used in Figure 4. The analytic Fourier series for this unit cell can be shown to be given by a sinc function in both x and y , much like the box function in 1D.

The calculated band structure for this crystal also converges as the harmonics increase, and at 25 harmonics the result is as shown in Figure 13. Again, this shows good agreement with J. Joannopoulos – visually the band structure is similar, and the TE gap-midgap ratio calculated here of 0.170 is similar to the reference value of 0.189 [5, p72].

Finally, to show the method is applicable to non-square Bravais lattices, the band structure for a crystal with a hexagonal unit cell was calculated. Consider an infinite crystal of dielectric, with a triangular pattern of air holes drilled into it. Once again, the Fourier series for this follows a Bessel function (Appendix C).

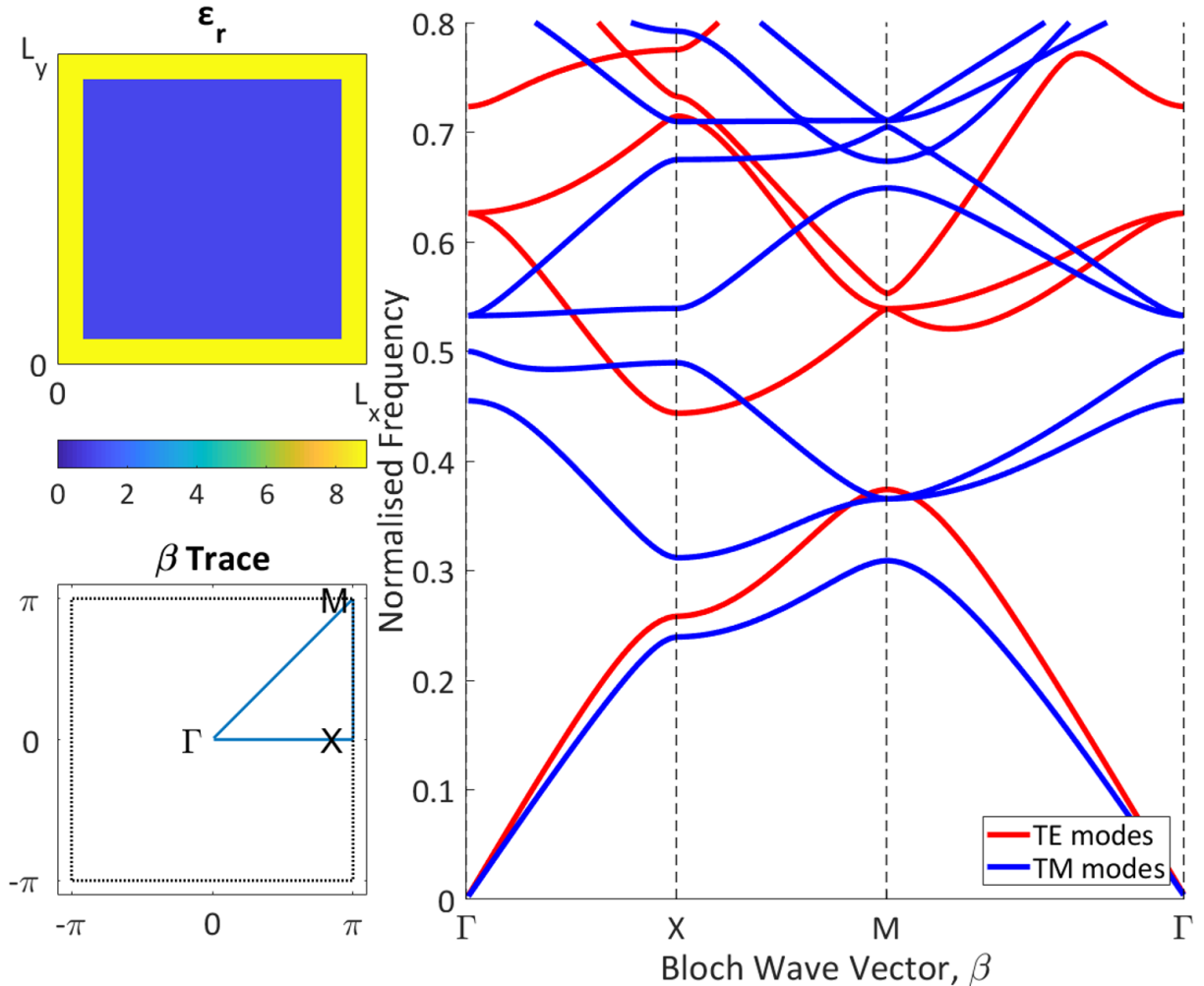


Figure 13: This shows the calculated band structure for the crystal of square air holes in dielectric ($\epsilon_r = 8.9$). There is not a complete band gap, but there is a partial band gap between the 1st and 2nd TE bands, giving a gap-midgap ratio of 0.1701.

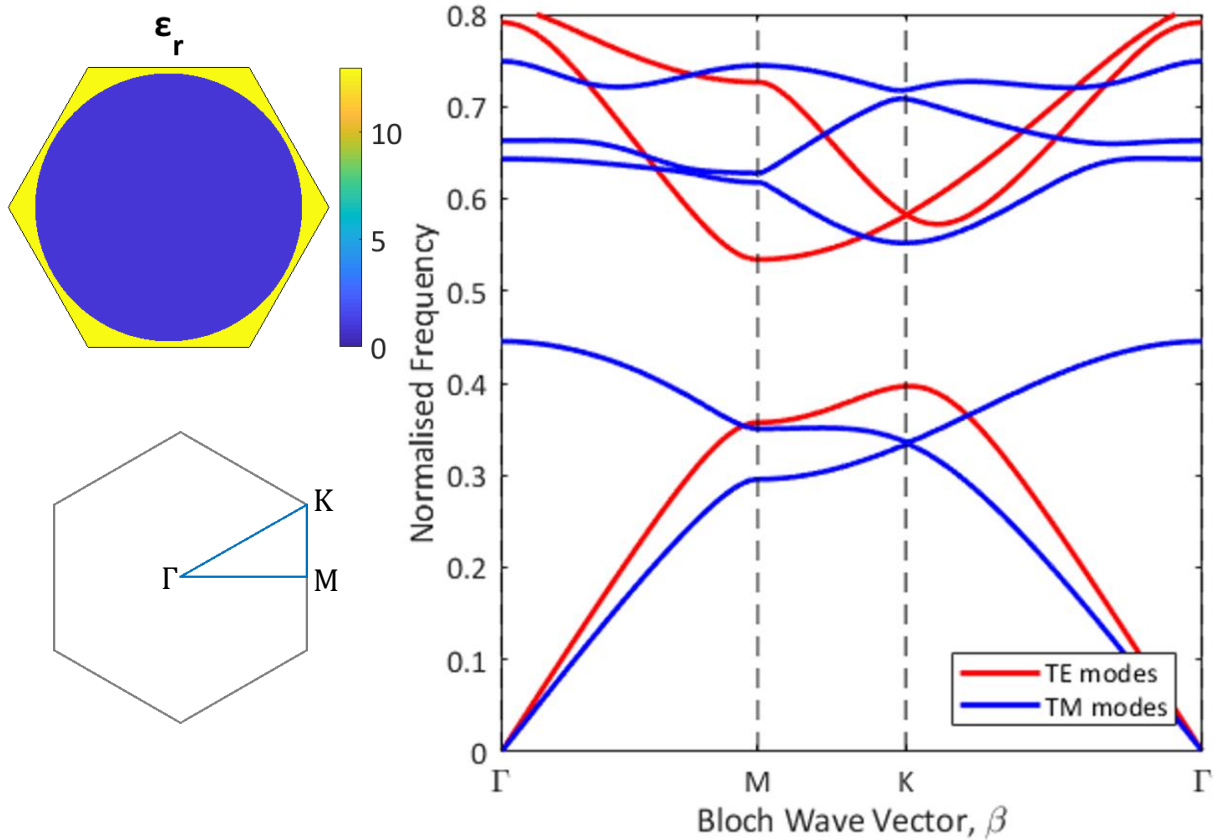


Figure 14: This shows the calculated band structure for the crystal of circular air holes ($r = 0.48L$) in dielectric ($\epsilon_r = 13$), for 35 harmonics. The predicted band gap around 0.5 has a gap-midgap ratio of 0.1813 – a little smaller than in the literature [5, p76].

The calculated band structure for this crystal is given in Figure 14 for 35 harmonics – 1225 plane waves. This crystal converges much more slowly than the other crystal – while there is reasonable agreement between this band structure and that given by J. Joannopoulos [5, p76], the agreement is not perfect, for example the shape of the 3rd and 4th TM band between Γ and M is notably different to that of the reference band structure. That being said, the predicted gap-midgap ratio of 0.181 is very close to his calculation of 0.186.

The reason for this slow convergence is not known, though perhaps may be related to the eigenvectors on either side of eigenvalue problem being in different bases.

5. Rumpf Implementation

This method was principally described by R. Rumpf in his lectures on computational electrodynamics [9,10,11]. The Rumpf implementation constructs the eigenproblem differently. Instead of creating a second order differential equation, as in Equations (3-4), consider the components of $\nabla \times \underline{E}$ and $\nabla \times \underline{H}$ independently. To simplify a few constants, a new field is defined:

$$\tilde{\underline{H}} = -i \sqrt{\frac{\mu_0}{\epsilon_0}} \underline{H} = -i\mu_0 c \underline{H} \quad (17)$$

Substituting this into Equation (2) then gives

$$\nabla \times \underline{\mathbf{E}} = k_0 \mu_r \tilde{\underline{\mathbf{H}}}, \quad \nabla \times \tilde{\underline{\mathbf{H}}} = k_0 \varepsilon_r \underline{\mathbf{E}} \quad (18)$$

Now, since $\tilde{\underline{\mathbf{H}}}$, $\underline{\mathbf{E}}$, μ_r and ε_r all vary in physical space, the products $\mu_r \tilde{\underline{\mathbf{H}}}$ and $\varepsilon_r \underline{\mathbf{E}}$ both become a convolution in reciprocal space, i.e. when the equations are Fourier transformed. Taking the z component of $\nabla \times \tilde{\underline{\mathbf{H}}}$ as an example (and dropping β subscripts for clarity):

$$k_x h_y(\underline{\mathbf{G}}) - k_y h_x(\underline{\mathbf{G}}) = ik_0 a(\underline{\mathbf{G}}) * e_z(\underline{\mathbf{G}}) = ik_0 \sum_{\underline{\mathbf{G}'}} a(\underline{\mathbf{G}} - \underline{\mathbf{G}'}) e_z(\underline{\mathbf{G}'}), \quad (19)$$

where $\underline{\mathbf{k}} = \underline{\beta} + \underline{\mathbf{G}}$. Combining the values of $e_z(\underline{\mathbf{G}'})$ for each $\underline{\mathbf{G}'}$ into a vector, $\underline{\mathbf{e}}_z$ (as in Figure 15), and similarly for the other components of $\underline{\mathbf{e}}(\underline{\mathbf{G}})$ and $\underline{\mathbf{h}}(\underline{\mathbf{G}})$, this can be rewritten as the matrix equation

$$\underline{\mathbf{k}}_x \underline{\mathbf{h}}_y - \underline{\mathbf{k}}_y \underline{\mathbf{h}}_x = ik_0 [\varepsilon_r] \underline{\mathbf{e}}_z \quad (20)$$

where $[\varepsilon_r]$ is the convolution matrix for the Fourier components of ε_r , and $\underline{\mathbf{k}}_x$, $\underline{\mathbf{k}}_y$ are diagonal matrices containing the k_x and k_y values for each $\underline{\mathbf{G}}$. For details of how to construct $[\varepsilon_r]$, see Figure 16.

Applying this to all 3 components of $\underline{\mathbf{E}}$ and $\tilde{\underline{\mathbf{H}}}$, and using the fact that the crystal is 2D (i.e. uniform in z), Equations (18) become the following 6 matrix equations.

$$\underline{\mathbf{k}}_y \underline{\mathbf{h}}_z = ik_0 [\varepsilon_r] \underline{\mathbf{e}}_x, \quad \underline{\mathbf{k}}_y \underline{\mathbf{e}}_z = ik_0 [\mu_r] \underline{\mathbf{h}}_x \quad (21)$$

$$-\underline{\mathbf{k}}_x \underline{\mathbf{h}}_z = ik_0 [\varepsilon_r] \underline{\mathbf{e}}_y, \quad -\underline{\mathbf{k}}_x \underline{\mathbf{e}}_z = ik_0 [\mu_r] \underline{\mathbf{h}}_y \quad (22)$$

$$\underline{\mathbf{k}}_x \underline{\mathbf{h}}_y - \underline{\mathbf{k}}_y \underline{\mathbf{h}}_x = ik_0 [\varepsilon_r] \underline{\mathbf{e}}_z, \quad \underline{\mathbf{k}}_x \underline{\mathbf{e}}_y - \underline{\mathbf{k}}_y \underline{\mathbf{e}}_x = ik_0 [\mu_r] \underline{\mathbf{h}}_z \quad (23)$$

Note that one half of these are in terms of $\underline{\mathbf{e}}_z$, and the other half in $\underline{\mathbf{h}}_z$. This means the TE and TM modes naturally fall out of the equations. Rearranging to eliminate $\underline{\mathbf{e}}_x$, $\underline{\mathbf{e}}_y$, $\underline{\mathbf{h}}_x$ and $\underline{\mathbf{h}}_y$, the eigenfunction formulation is finally obtained.

$$(\underline{\mathbf{k}}_x [\mu_r]^{-1} \underline{\mathbf{k}}_x + \underline{\mathbf{k}}_y [\varepsilon_r]^{-1} \underline{\mathbf{k}}_y) \underline{\mathbf{e}}_z = k_0^2 [\varepsilon_r] \underline{\mathbf{e}}_z \quad (24)$$

$$(\underline{\mathbf{k}}_x [\varepsilon_r]^{-1} \underline{\mathbf{k}}_x + \underline{\mathbf{k}}_y [\varepsilon_r]^{-1} \underline{\mathbf{k}}_y) \underline{\mathbf{h}}_z = k_0^2 [\mu_r] \underline{\mathbf{h}}_z, \quad (25)$$

where $[\varepsilon_r]^{-1}$ is the inverse of the convolution matrix. Note these equations are of the form $\underline{\mathbf{A}} \underline{\mathbf{v}} = \lambda \underline{\mathbf{B}} \underline{\mathbf{v}}$, but are still solvable numerically using the MATLAB ‘eig’ function. The eigenvalues are again k_0^2 , and so must be changed to the normalised frequency in the same way as for the semi-analytic method, Equation (15). These equations also reflect the inherent symmetry in Maxwell’s equations between magnetic and electric fields, making this an aesthetically pleasing eigenproblem formulation.

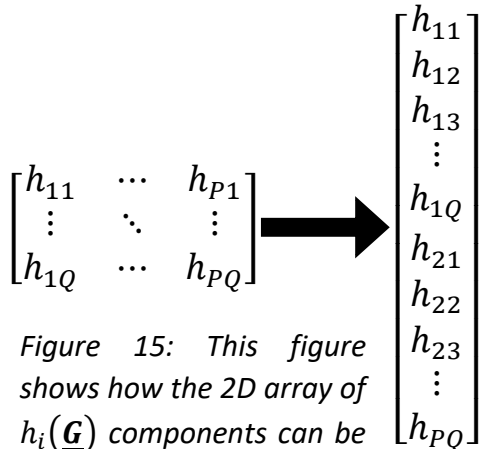


Figure 15: This figure shows how the 2D array of $h_i(\underline{\mathbf{G}})$ components can be expressed as a 1D vector.

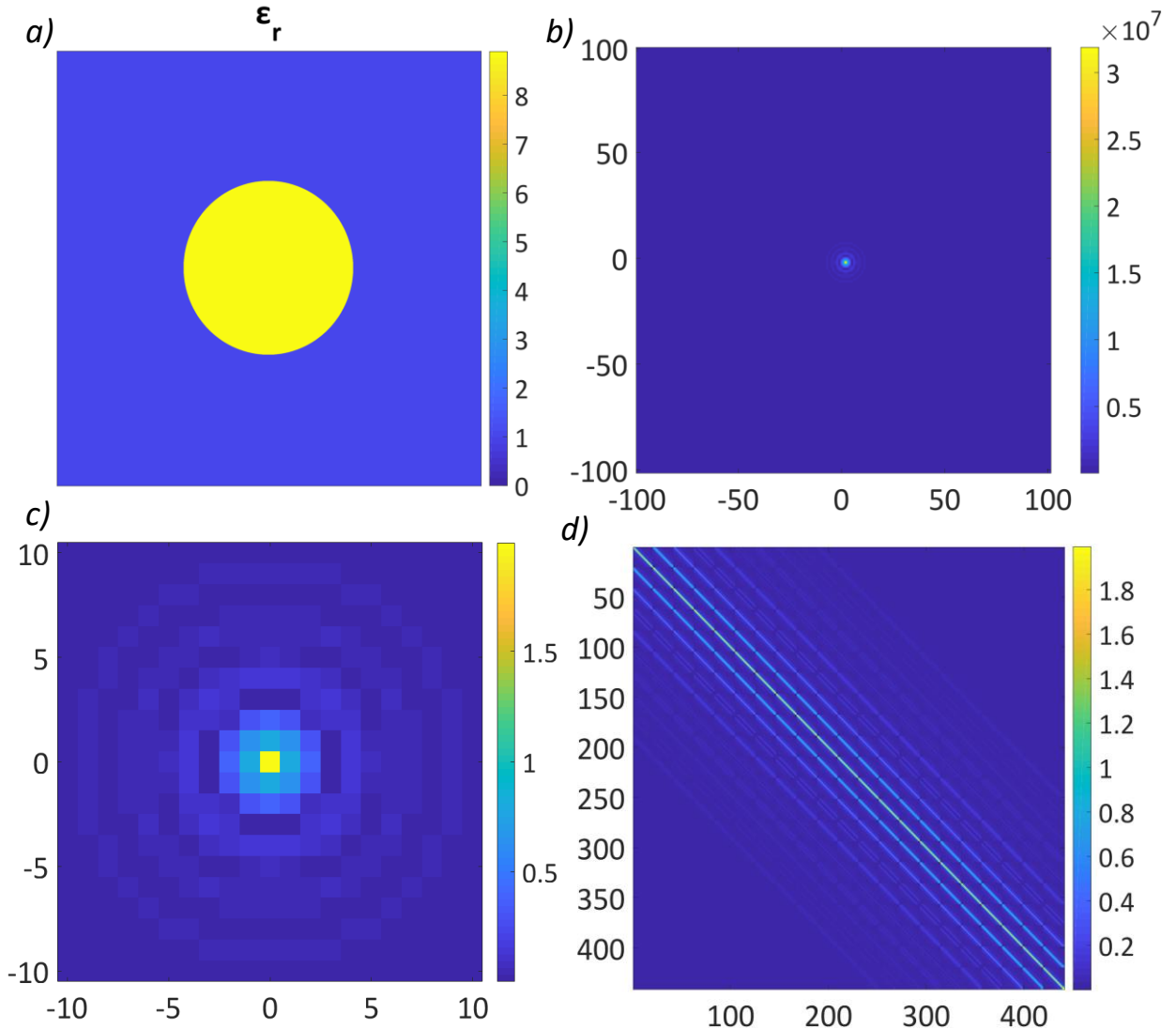


Figure 16: This figure shows how the convolution matrix is built from the FFT of the unit cell. a) shows a high resolution (4000×4000) approximation of the ϵ_r of a unit cell. The 2D FFT of this is a 4000×4000 array of complex values, of which the magnitudes of the central 200×200 are shown in b). The central $P \times Q$ elements (21×21 in this case) are then extracted, and divided by the resolution of the unit cell to normalise the components, as shown in c). By rearranging the elements into a column vector as in e), the convolution matrix can be constructed, as in d). This is equivalent to viewing c) as a list of Fourier components for reciprocal lattice vectors, \underline{G} , and d) as the table of Fourier coefficients for all $\underline{G} - \underline{G}'$. For a more explicit explanation of how to build this computationally, see Rumpf description [9, pp 14-20].

The Rumpf method does not make any assumptions about the permeability or permittivity of the unit cell, making it more general than the semi-analytic method, but unfortunately the method given by Rumpf for constructing the convolution matrices, $[\epsilon_r]$ and $[\mu_r]$, uses a rectangular grid to store a high resolution approximation of the unit cell, and utilises the FFT on this grid to obtain the Fourier series for the unit cell (see Figure 16). This does introduce errors into the calculation, as the Fourier coefficients obtained this way are not exactly the same as those of the infinite Fourier series. In this project, a minimum of 1000 grid elements

were used in each direction. For P and $Q \leq 21$ (i.e. $-10 - 10$), this gives the grid at least 100 times more spatial precision than the truncated Fourier series, making the FFT a good approximation to the infinite Fourier series. The error in this will be negligible compared to the error caused by the Fourier series truncation itself. Unfortunately, the FFT limits the method as described by Rumpf to applying only on rectangular Bravais lattices – rectangular unit cells [9, pp 14-20].

However, recent work by J. Birdsong and N. Rummelt has enabled the calculation of the Fast Fourier Transform of a hexagonal lattice as well [12]. This ‘Hexagonal Fast Fourier Transform’ (HFFT) was implemented in MATLAB according to their specifications, and the method to calculate the convolution matrix modified to use the new technique and associated data structures (see Appendix D for details). A variant of the Rumpf method was constructed using these tools instead of the original rectangular basis FFT.

Thus, the Rumpf method should be applicable to any photonic crystal with either rectangular or hexagonal Bravais lattices. In principle, centred rectangular lattices should also be possible, but such a unit cell would not be primitive, adding an additional layer of complexity which will be discussed later (Section 7).

By the nature of the eigenproblem formulation, this method takes advantage of MATLAB’s efficient matrix operations. As such there is little improvement to make to the efficiency of the code, beyond utilising parallel processing to solve the eigenproblem for multiple β s simultaneously. Because this method does not assume $\mu_r = 1$, constructing the eigenproblem matrices will take longer than for the semi-analytic method, but this is insignificant compared to the time taken to solve the eigenproblem itself. This is because the eigenproblem is in a more complex form, $A\underline{v} = \lambda B\underline{v}$, than the semi-analytic method ($A\underline{v} = \lambda \underline{v}$). For identical crystals and harmonics, the Rumpf method takes approximately 4 times longer to calculate the band structure.

6. Rumpf Results

One key advantage of the Rumpf method is that it does not require the Fourier series to be analytic. This allows different crystals and variations of crystals to be tested quickly without needing to manually rederive the Fourier series each time. As before, to be confident the calculator is accurate, the calculated band structure must be shown to converge for higher harmonics and shown to agree with the existing literature.

Once again, consider a square unit cell of air with a circular column of dielectric, as for the semi-analytic method in Figure 11. Calculating the band structure for this using the Rumpf method again gives good agreement with J. Joannopoulos [5, p68] (see Figure 17).

Physically, it should not matter where in the unit cell the column lies – the same infinite crystal will be formed from it regardless. Whether our calculator respects this symmetry can be easily tested by changing the high-resolution grid to one with the circle offset. The calculation for such a crystal is shown in Figure 18.

This offset cell band structure is identical to the non-offset version. However, the band structure only shows the eigenvalues to the eigenproblem, not the eigenvectors. Plotting the electric fields that are associated with the 7th TE bands at Γ in each case shows how the offset has changed the eigenproblem (see Figure 19). This was done by taking the inverse Fourier transformation of the corresponding eigenvector in each case (after rearranging it from a P^2 column vector into its $P \times P$ square array form, Figure 20). Translating the unit cell features simply applies a phase shift to the resulting fields' Fourier components.

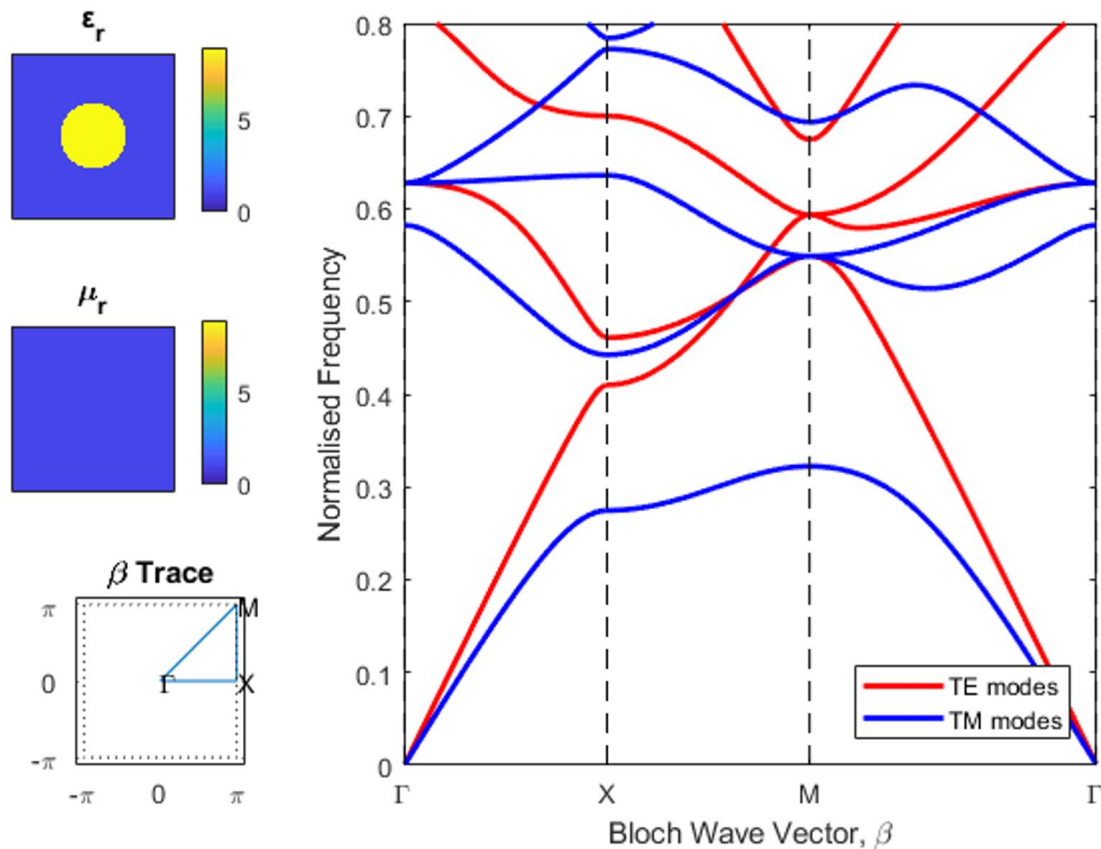


Figure 17: This shows the calculated band structure for a circular dielectric column, $\epsilon_r = 8.9$, $r = 0.2L_x$, in a square unit cell, using the Rumpf method and 17 harmonics. Very strong agreement is found with Figure 12, and J. Joannopoulos [5, p68].

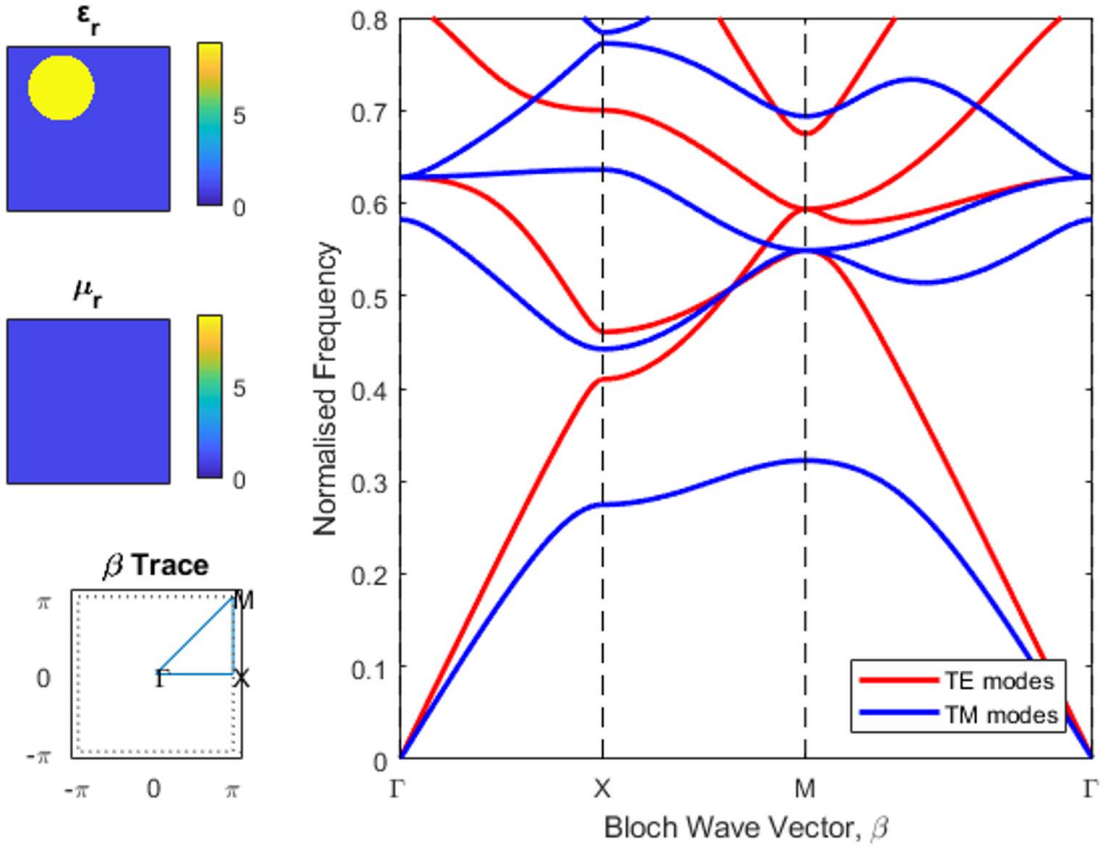


Figure 18: This figure shows the calculated band structure for an offset circular dielectric column, with all other properties the same as in Figure 17. The calculated band structure is identical to that in Figure 17.

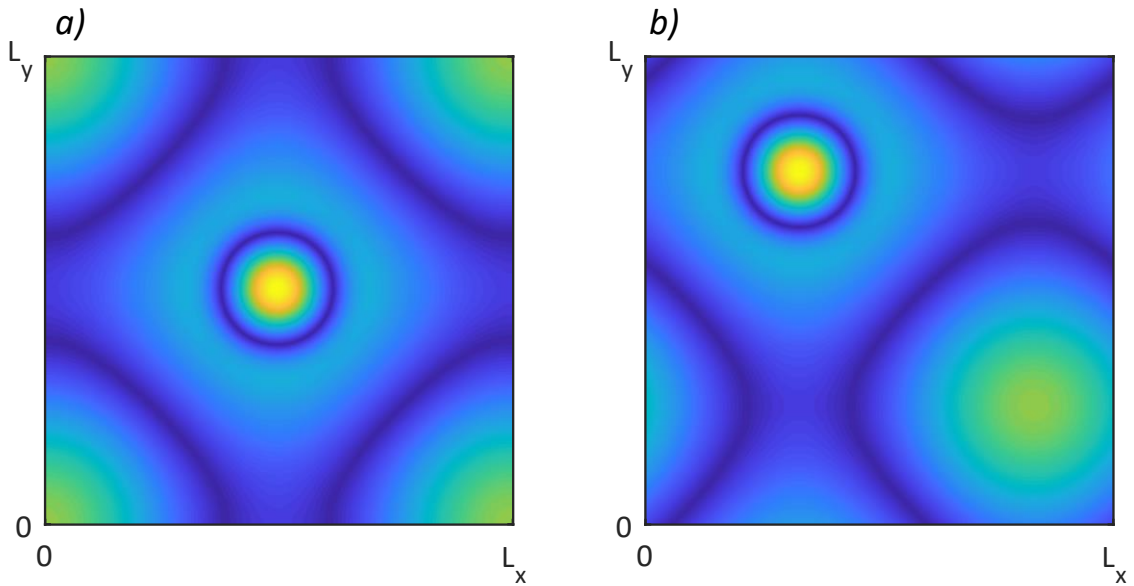


Figure 19: This figure shows magnitude of the electric field associated with the 7th TE band at Γ across the entire unit cell for the centred and offset unit cells in a) and b) respectively. Note the offset between the two fields matches the offset of the unit cell. The 7th TE band was chosen purely for aesthetic purposes – all of the fields show the same offset.

Next, consider the square air hole in dielectric unit cell, the same as in Figure 13 for the semi-analytic method. The calculated band structure for this unit cell with the Rumpf method is shown in Figure 21. Again, very strong agreement is found with both the semi-analytic method and with J. Joannopoulos [5, p72].

As mentioned in Section 5, there is a symmetry in the source-less Maxwell's equations between the magnetic and electric fields. This implies that if the ϵ_r and μ_r for a unit cell were swapped, then the fields would also swap – the TE and TM bands would switch places.

$$\begin{bmatrix} h_{11} \\ h_{12} \\ h_{13} \\ \vdots \\ h_{1Q} \\ h_{21} \\ h_{22} \\ h_{23} \\ \vdots \\ h_{PQ} \end{bmatrix} \xrightarrow{\text{black arrow}} \begin{bmatrix} h_{11} & \cdots & h_{P1} \\ \vdots & \ddots & \vdots \\ h_{1Q} & \cdots & h_{PQ} \end{bmatrix}$$

Figure 20: This shows the rearrangement of the eigenvector components necessary to get it back into the form of a 2D Fourier series. To use this with the MATLAB inverse FFT, it must be centred in an array of the same size as the desired final image.

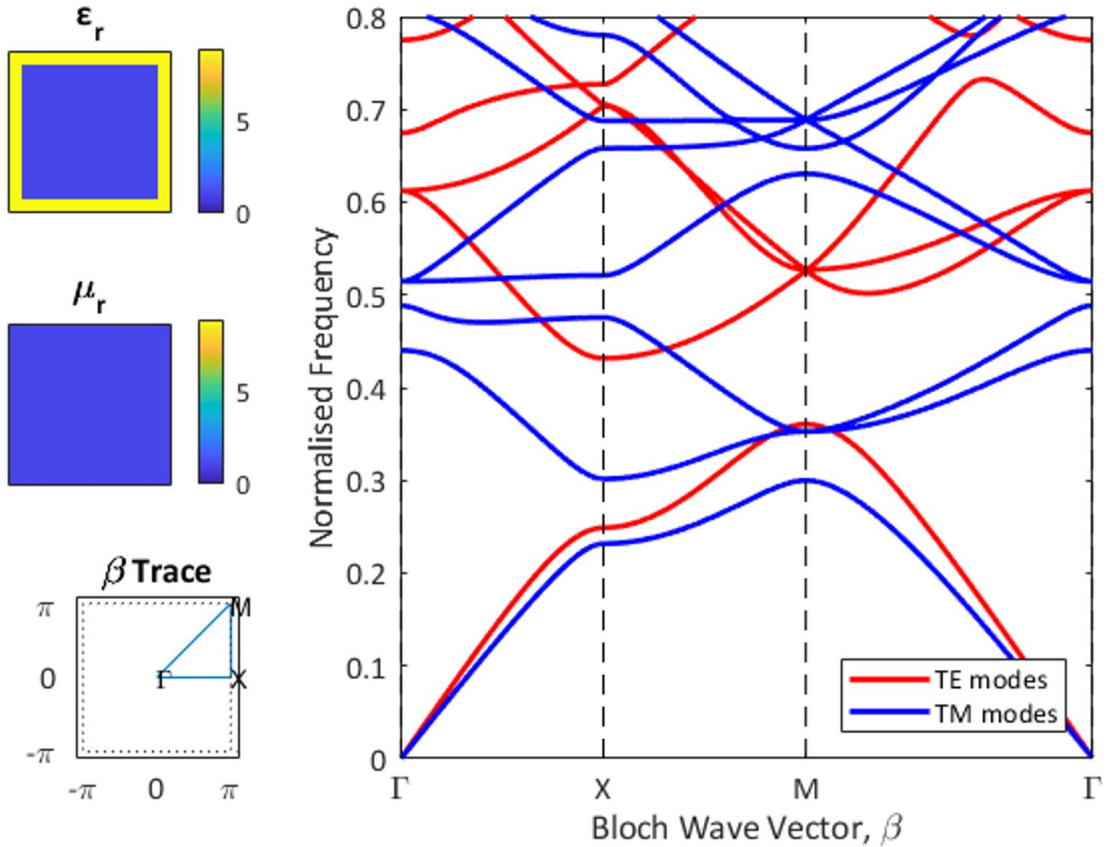


Figure 21: This figure shows the calculated band structure for a dielectric material, $\epsilon_r = 8.9$, with a square air hole drilled into it, width = $0.835L_x$, in a square unit cell using the Rumpf method and 17 harmonics. This has very strong agreement with both Figure 13 and the band structure given by J. Joannopoulos for this crystal [5, p72].

With the Rumpf method, this symmetry can now be tested. The ϵ_r and μ_r of the square air hole unit cell were swapped, and the band structure for the new crystal calculated (see Figure 22) As expected, the TE and TM bands were swapped as compared to the band structure shown in Figure 21.

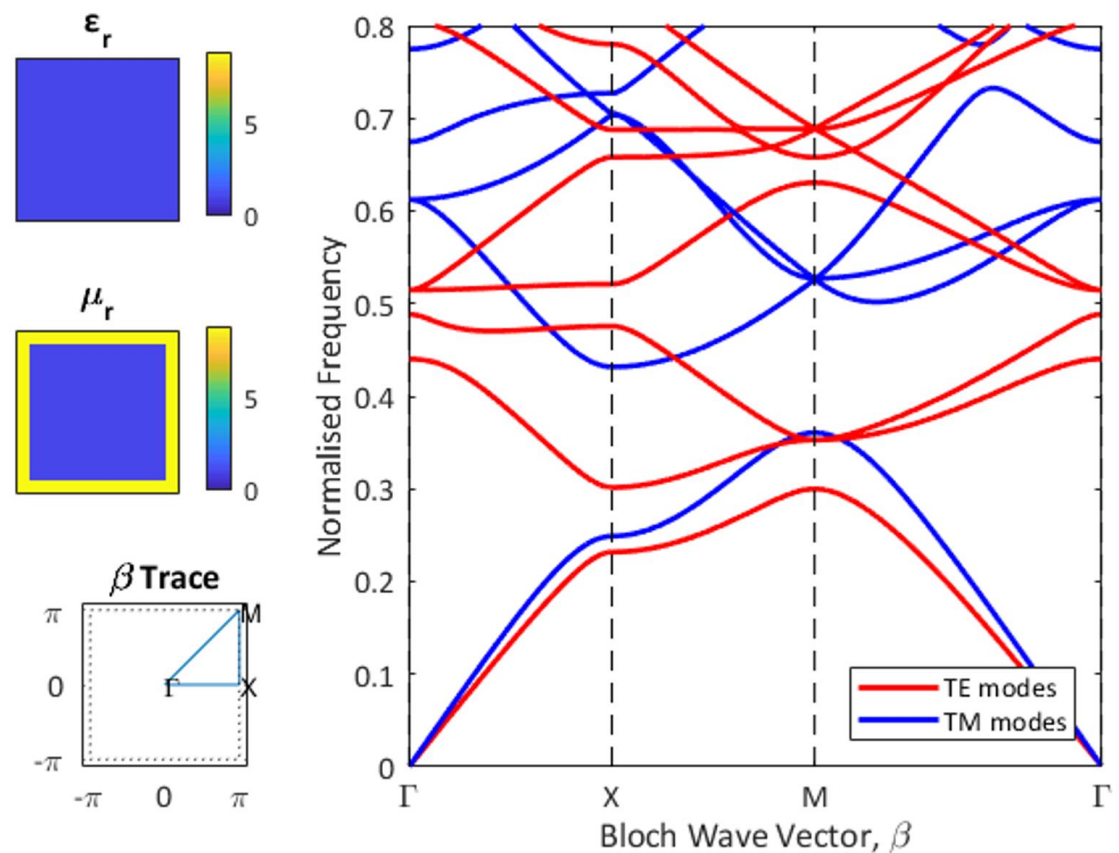


Figure 22: This figure shows the calculated band structure for a magnetic material, $\mu_r = 8.9$, with a square air hole drilled into it, width = $0.835L_x$. As in Figure 21, 17 harmonics are used. The band structure is identical to Figure 21, except for the TE and TM bands being swapped.

So far, all the unit cells that have been tested have only two materials in them. While this is usually sufficient for current photonic crystals, it is worth verifying the calculator is accurate for more elaborate crystals. In ‘Photonics: Optical Electronics in the Modern World’, A. Yariv analytically calculates the TM modes for such a crystal [13, p597]. Calculating the band structure for this crystal gives extremely good agreement with Yariv’s results, and also provides the corresponding TE modes (see Figure 23). The 1st TM band gap was calculated to be over the range 0.258-0.283 – identical to the range of frequencies calculated by A. Yariv.

Similarly, all of the unit cells tested so far are square. To be confident in the calculator, it should be tested both with a rectangular unit cell, and with a hexagonal unit cell using the HFFT variant.

For a rectangular cell, consider the optimised cell given by M. Qui in his paper, “Large complete band gap in two-dimensional photonic crystals with elliptic air holes” [14]. Calculating this band structure initially did not give good agreement with M. Qui, as there was an error in the code when building the \mathbf{k}_x and \mathbf{k}_y matrices. This error went unnoticed as it only caused the calculated eigenvalues (and so the band structure) to be affected if the lengths of the reciprocal lattice vectors, $\underline{\mathbf{b}}_1$ and $\underline{\mathbf{b}}_2$, were different.

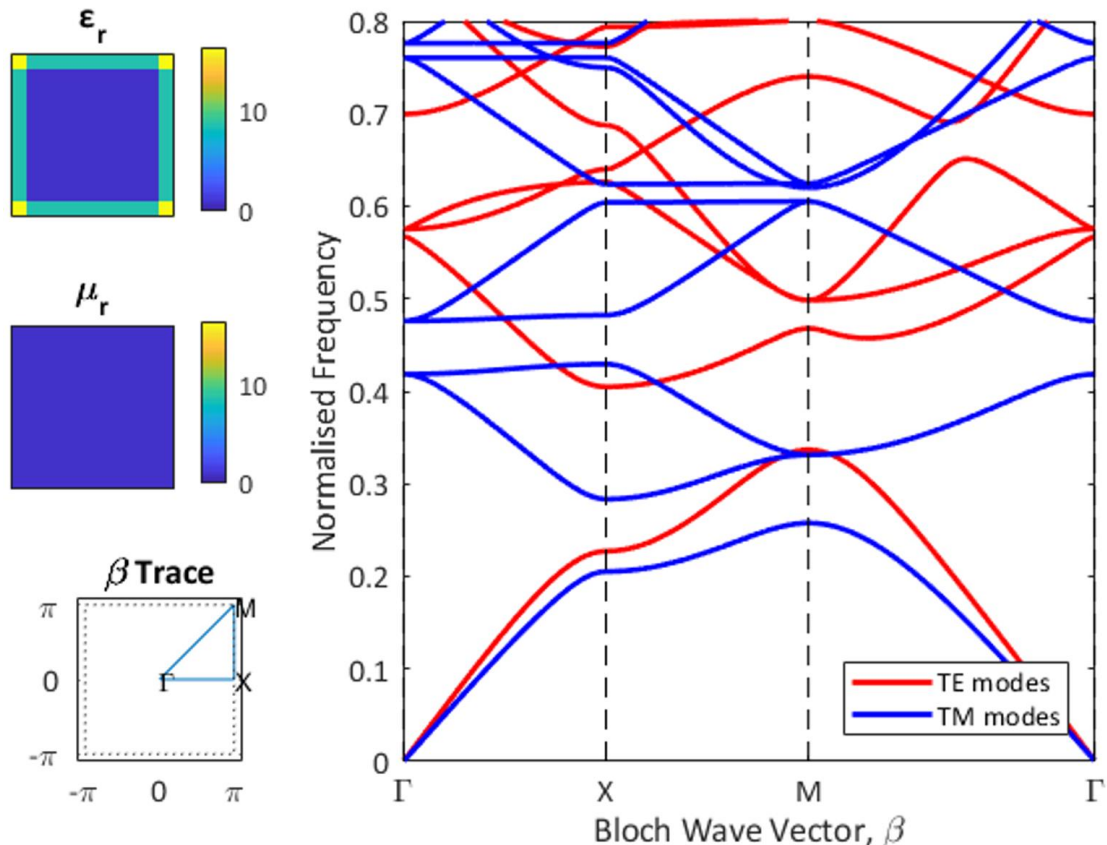


Figure 23: This figure shows the calculated band structure for a square unit cell with three materials, a square air hole of width = $0.8L$ in the centre, four $0.8L \times 0.1L$ regions of $\epsilon_r = 8.7$, and the remaining four corners having $\epsilon_r = 16.4$. 21 harmonics were used to calculate this band structure, and good agreement is found with Yariv for the TM bands [[g], p597]. The 1st TM band gap spans the range 0.2577-0.2834.

Once this error was corrected, the calculator gave the band structure shown in Figure 24. For a rectangular unit cell, the IBZ becomes a quarter of the 1st BZ. As such, the M- Γ path included in this figure is not strictly on the perimeter of the IBZ, and does not correspond to any symmetry. However, it is included here to keep the calculated band structure as similar as possible to the literature band structure. It was calculated for 21 harmonics, corresponding to 441 plane waves – the same number as in M. Qui’s calculations. However, a much smaller band gap was predicted using this method than given by M. Qui – only 0.0082 to his 0.0304. Given the narrowest feature in the x direction is 10 times narrower than the narrowest y direction feature ($0.01L_y$ to $0.1L_y$), it was attempted to rebalance the harmonics to reflect this. The calculation was repeated with $P = 63$ and $Q = 7$ (and the resolution of the unit cell grid increased to keep it much larger than the number of harmonics). However, the new band structure was not visually distinct from the original, with the band gap only widening by about 10% to 0.0091 – still more than 3 times narrower than M. Qui’s prediction.

While the width of the band gap does not match, the shape of the bands has very good agreement. This difficulty verifying M. Qui’s band gap has also been experienced by others [15].

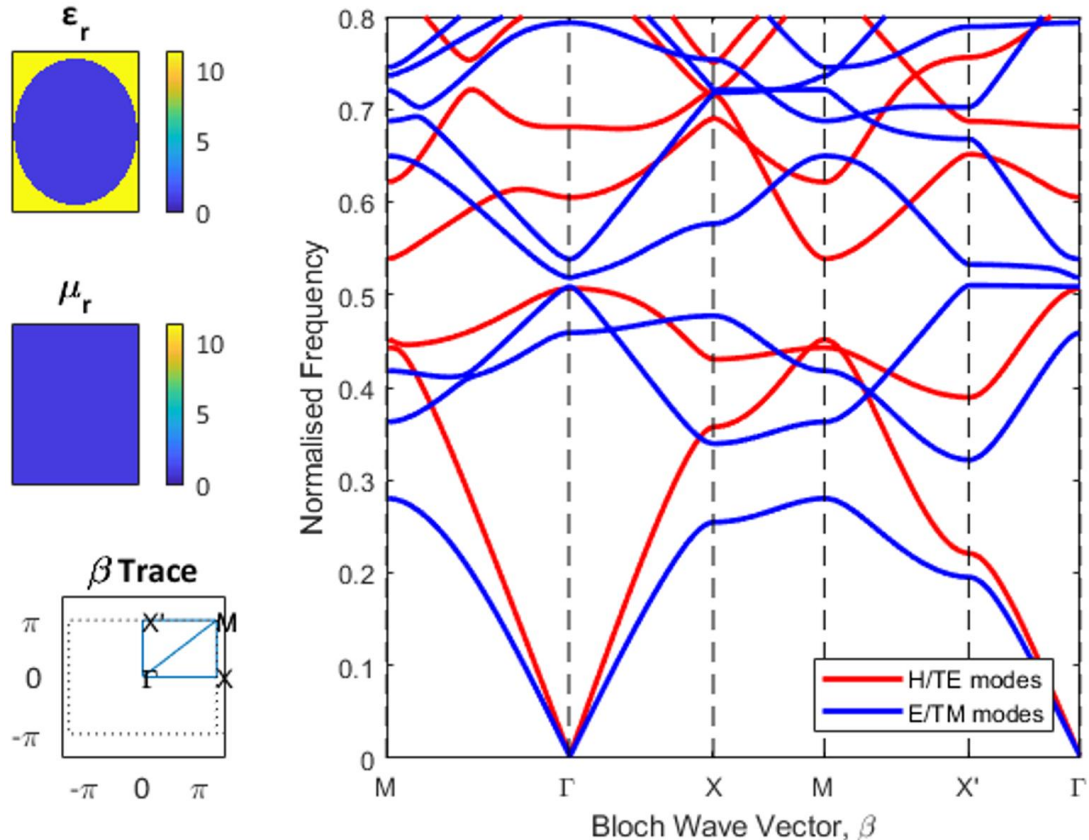


Figure 24: This figure shows the band structure calculation for a 0.77×1 rectangular dielectric crystal cell ($\epsilon_r = 11.4$), with a 0.76×0.9 elliptical air hole drilled into it. This calculation was done with $P = Q = 21$. Note the narrow band gap around 0.51 of only 0.0082, much less than the 0.0304 predicted by M. Qui [14].

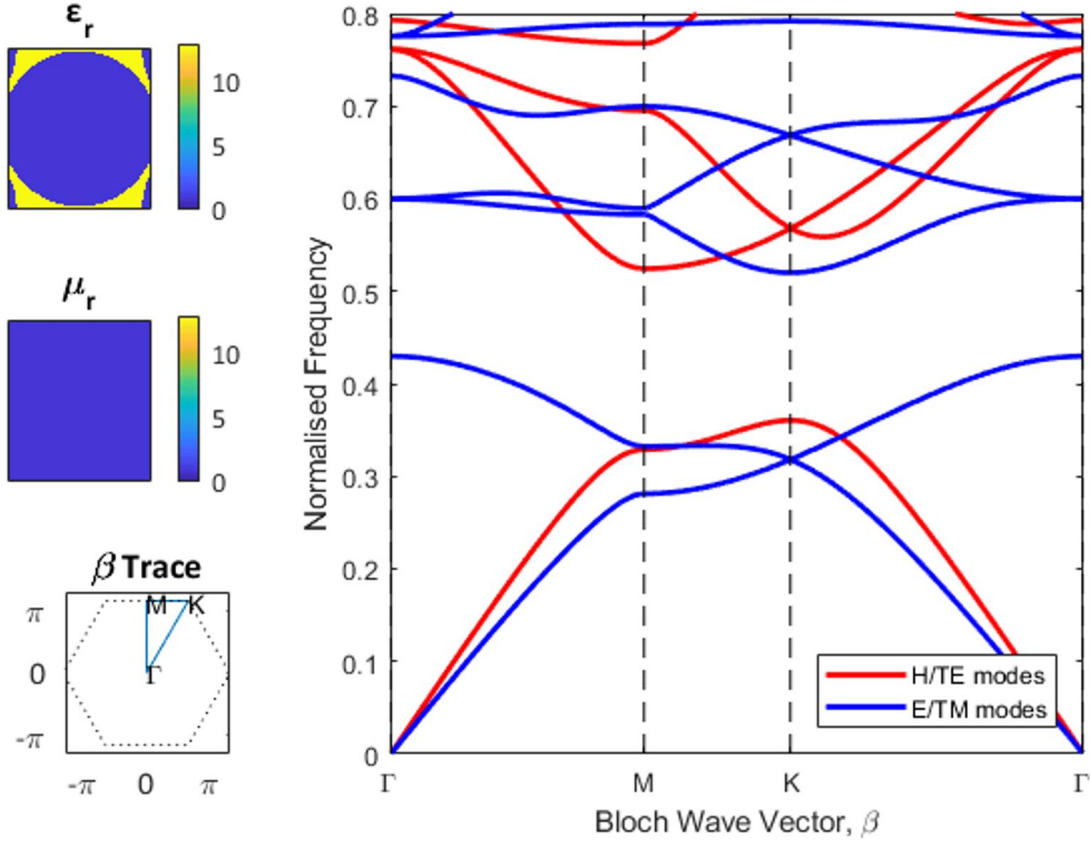


Figure 25: This figure shows the band structure for a hexagonal unit cell of dielectric ($\epsilon_r = 13$) with a circular air hole drilled into it ($r = 0.48L$). On the path between two adjacent lattice vectors, 96% of the path is in air. This band structure is calculated with 21 harmonics, and predicts a band gap of 0.0902, or a $\Delta\omega/\omega_m = 0.1899$, very close to the 0.186 predicted by J. Joannopoulos [5, p75]. Note the unit cell is presented as a rectangle in ASA coordinates, as described by J. Birdsong and N. Rummelt [12], and Appendix D.

Finally, the HFFT variant of the method was verified by testing the circular air hole in a hexagonal cell again. Figure 25 shows the calculated band structure for this unit cell, and the layout of the unit cell in the hexagonal ASA coordinates. This calculated band structure has excellent agreement with J. Joannopoulos's calculation [5, p76], with a predicted $\Delta\omega/\omega_m$ of 0.190, very close to his 0.186 result.

The agreement of this method with the literature for this crystal is also clearly far superior to the semi-analytic method, even with substantially fewer harmonics being used. The reason for this is as yet unclear. Utilising the HFFT instead of the analytic Fourier components does not change the band structure calculated by the semi-analytic method.

7. Non-Primitive Unit Cells

A couple of naïve attempts at calculating the band structure for multiple unit cells can be seen in Figure 26. While both are clearly incorrect, they give a hint for where the problem arises. The 1D double cell predicts band gaps in the right places, and the 2D quadruple cell appears to have two bands merging into one at X . When a unit cell is repeated, the code will calculate the reciprocal lattice vectors for the unit cell as if it were a primitive unit cell. Therefore, for the cases in Figure 26, the calculated reciprocal lattice vectors will all be half the length as for a primitive unit cell. This affects both the set of lattice vectors used to construct the eigenproblem, \mathbf{G} , and the path in reciprocal space Γ, X, M, Γ traversed by the Bloch wave vectors, β .

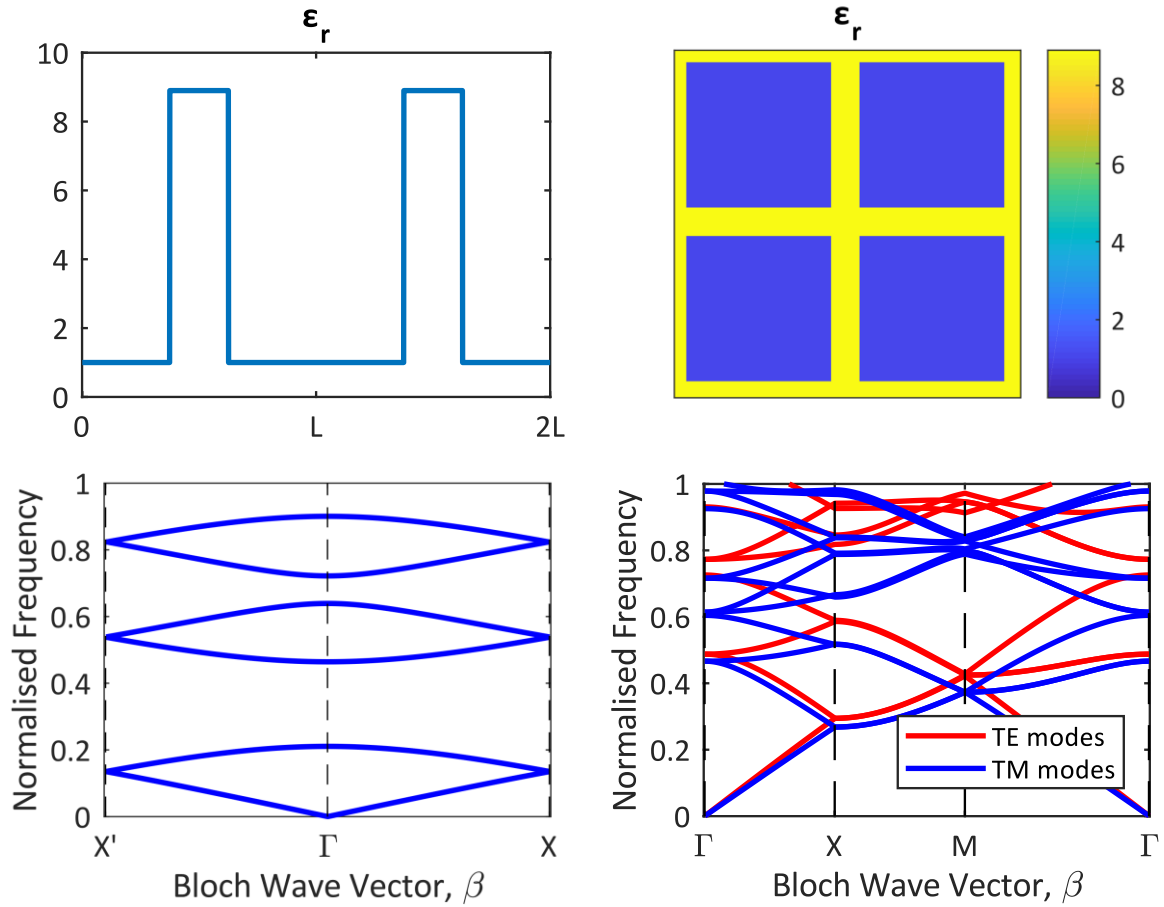


Figure 26: These plots show the produced band structures when a non-primitive unit cell is passed into the Rumpf calculator with no modifications to correct them. The upper plots show the unit cells, a double 1D cell and a quadruple 2D cell, and the lower plots show the corresponding band structure. The ‘true’ band structures for these non-primitive unit cells can be found in Figures 8 and 21 respectively.

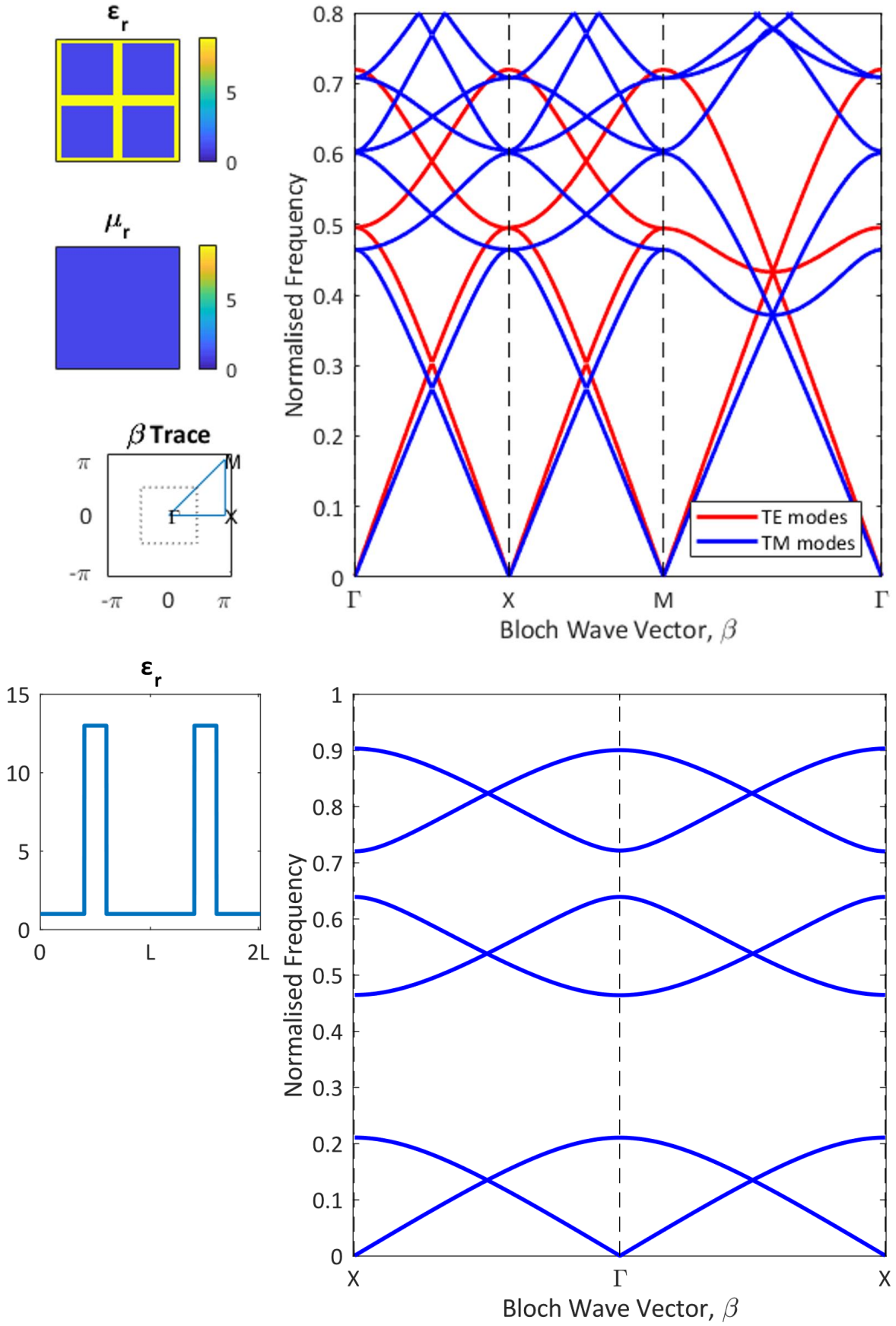


Figure 27: These plots show the band structures for the non-primitive unit cells from Figure 26, now with their Bloch wave vectors spanning twice the distances in reciprocal space.

The Bloch wave vectors can be easily corrected to travel the same path as that of the single unit cell. Doing this, the ‘true’ band structure becomes apparent, along with another set of bands, which R. Rumpf calls ‘Mystery Bands’ [10, p27] (see Figure 27).

To explain the origin of these mysterious non-physical bands, consider the double 1D unit cell, as in Figure 28. Taking the Fourier transform of this yields a sinc function again, but with each component spaced by an additional zero. This is consistent with the reciprocal lattice vector being halved – the non-zero points in reciprocal space now correspond to every other reciprocal lattice vector.

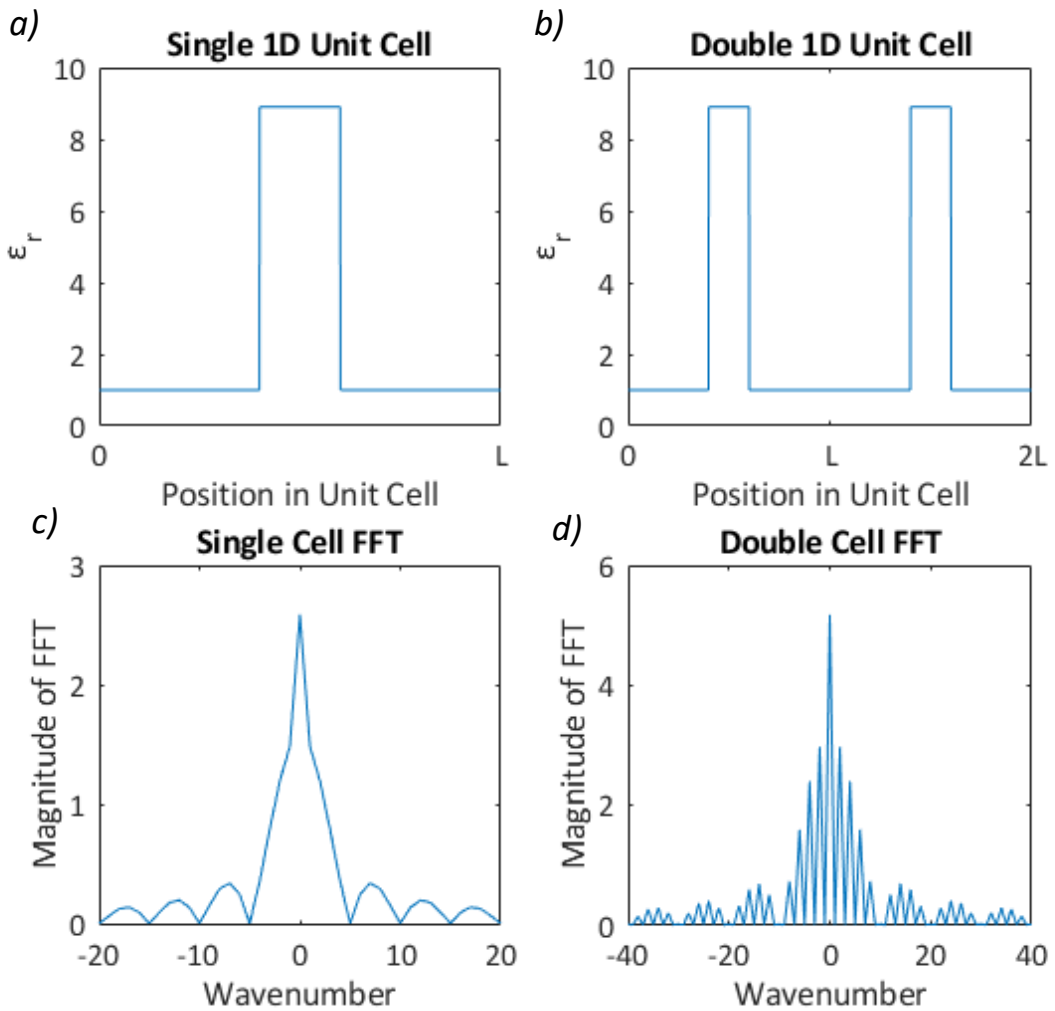


Figure 28: These plots show how the Fourier series for a unit cell changes when the unit cell is doubled. Graphs a) and b) show the single and double unit cells respectively, while c) and d) show the smallest 41 and 81 Fourier components for the single and double cells respectively. Note that every odd wavenumber for the double cell Fourier series has zero amplitude, corresponding to modes with a maximum in the middle of the double cell. Note also the envelope of the non-zero double cell wavenumbers match exactly the magnitudes of the single cell wavenumbers, modulo a factor of two in the magnitude and wavenumber.

The convolution matrix then takes this expanded Fourier series and interleaves it to create a kind of checkerboard pattern of non-zero elements (see Figure 29). As the eigenproblem is proportional to the convolution matrix, this allows for eigenvectors to exist which correspond to magnetic fields that do not adhere to the periodicity of the primitive unit cell, and instead are periodic on the double unit cell. These fields are not physically allowed as they destructively self-interfere, but they produce eigenvalues which the code will naively display.

Thankfully, these non-physical eigenvectors are straightforward to identify – the checkerboard pattern of the convolution matrix means that they have zero amplitude for every physically allowed Fourier component, at least up to a small numerical error in the eig function.

This same approach works with 2D crystals, though care must be taken as the structure of the convolution matrix is more complicated. The convolution matrix for a 1x2 double 2D unit cell as shown in Figure 30. The pattern here is not quite a checkerboard pattern, as it is only checkerboarded within each PxQ block. However, it is still a perfectly regular and predictable pattern, and so the non-physical eigenvectors can still be easily filtered out.

Discarding eigenvalues whose eigenvectors have a value of less than 10^{-10} for physically allowed Fourier components yields the band structure shown in Figure 31. Computationally this is most efficiently done by trimming the offending rows and columns out of the eigenproblem matrices before solving, as this saves the time needed to calculate the non-physical eigenvalues.

Often this is enough by itself, but sometimes the band structure disagrees with the literature band structure by some multiple. The problem is that the band structure is normalised by the length scale of the unit cell, usually L_x or L_y for a rectangular unit cell. However, when using a non-primitive unit cell, the length scale of the composite unit cell

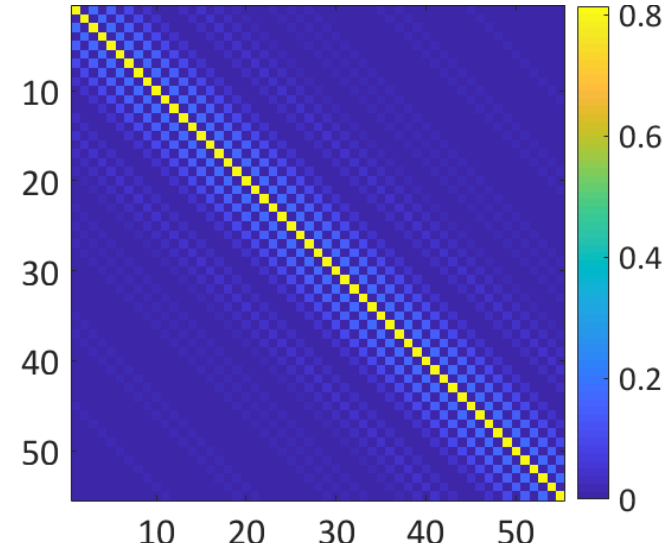


Figure 29: This shows the magnitude of each complex value in the convolution matrix for the double 1D unit cell used in Figures 26 and 27. Note that every other element is zero.

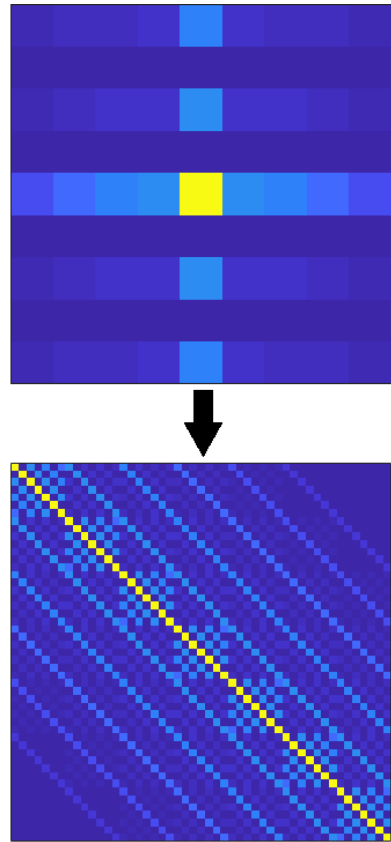


Figure 30: This shows the pattern of alternating rows of zeros for a 1x2 double 2D cell, and the resulting pattern this produces in the convolution matrix for 7 harmonics.

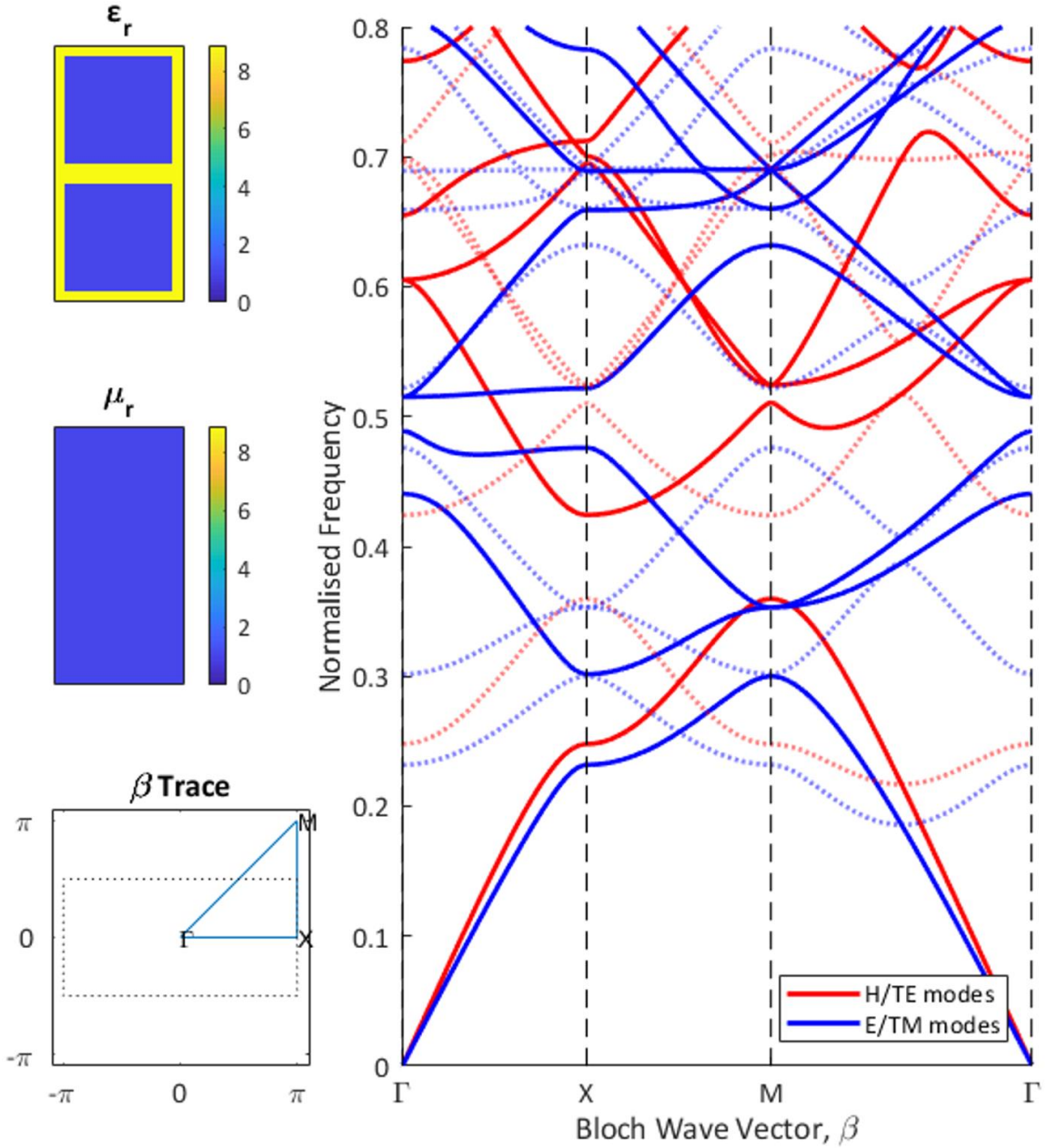


Figure 31: This figure shows the band structure for a double unit cell, where the non-physical ‘mystery’ bands have been identified, and are here plotted as semi-transparent dotted lines. Note the symmetry between real and mystery bands along the X-M path. This was calculated with 17 y harmonics and 9 x harmonics, giving an effective 9x9 harmonics for the real bands. This calculated band structure is thus similar to Figures 13 and 21, but for a smaller number of harmonics.

will not always match the length scale of the primitive unit cell, and so may need rescaling to match literature values.

It is important to note that by trimming non-physical eigenvalues, approximately half the frequencies solved for are thrown away – e.g. of the lowest 13 harmonics for a double cell, 6 are physically forbidden. To actually obtain the lowest 13 allowed modes, the convolution matrix would need to be calculated for the first 25 Fourier components of the double cell.

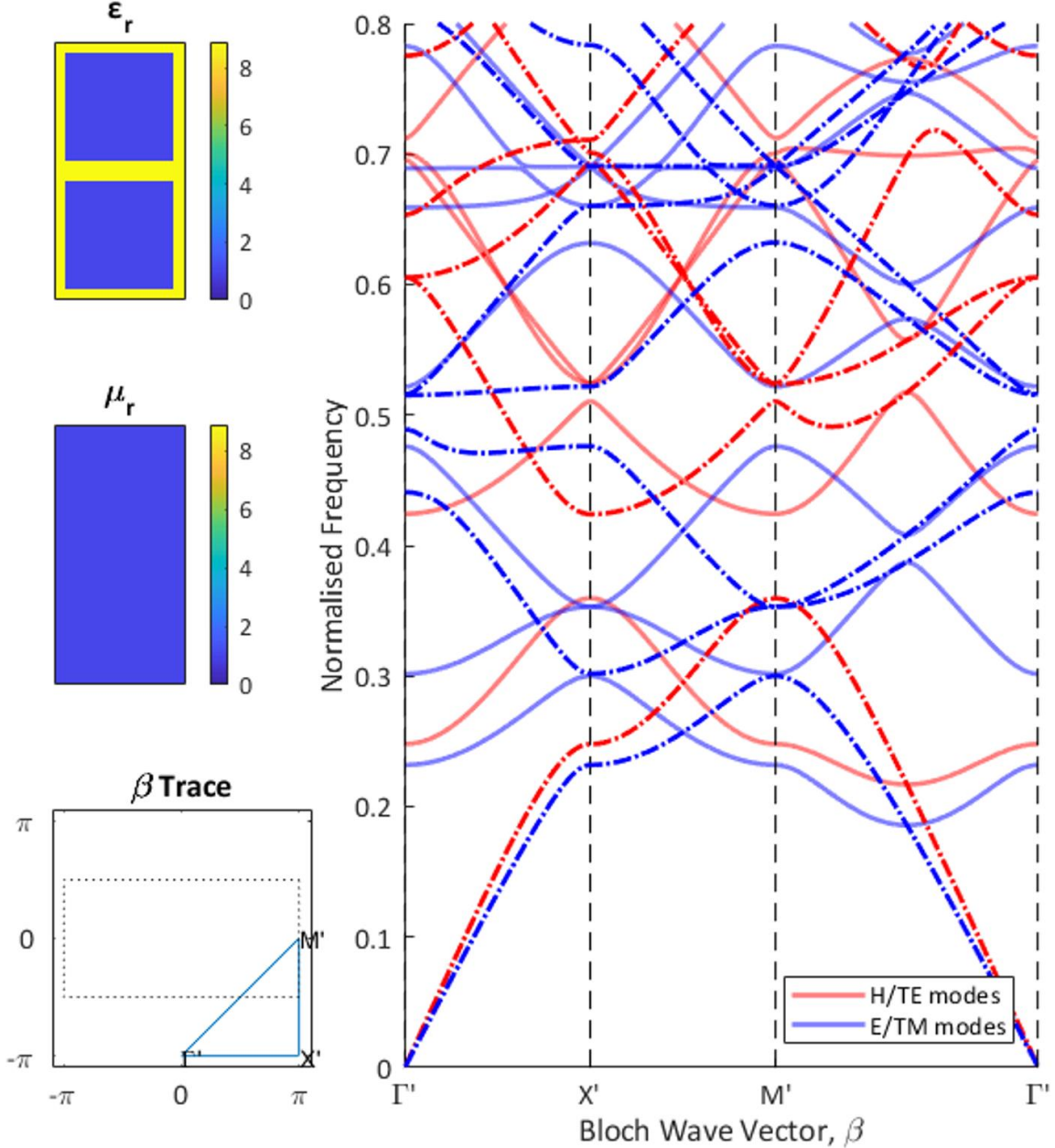


Figure 32: This figure shows the same crystal as Figure 31, except the trace of points in reciprocal space is changed to that corresponding to an adjacent BZ. This time the ‘real’ bands are semi-transparent lines, and the ‘mystery’ bands are dashed lines. This was again calculated with 17 y harmonics and 9 x harmonics, giving an effective 8x9 harmonics for the mystery bands.

An interesting side note is that the non-physical ‘mystery’ bands themselves give a copy of the true band structure, albeit centred off the ‘true’ grid, as hinted at by the symmetry for the 1D crystal band structure in Figure 27. Although their frequencies and wave vectors are not physical, tracing around the IBZ plus half a reciprocal lattice vector for the mystery bands gives the same band structure as the ‘real’ bands (see Figure 32). Perhaps this should not be very surprising as two BZs have been spanned over to find our ‘true’ band structure – finding a second copy of it in that space is a satisfying result.

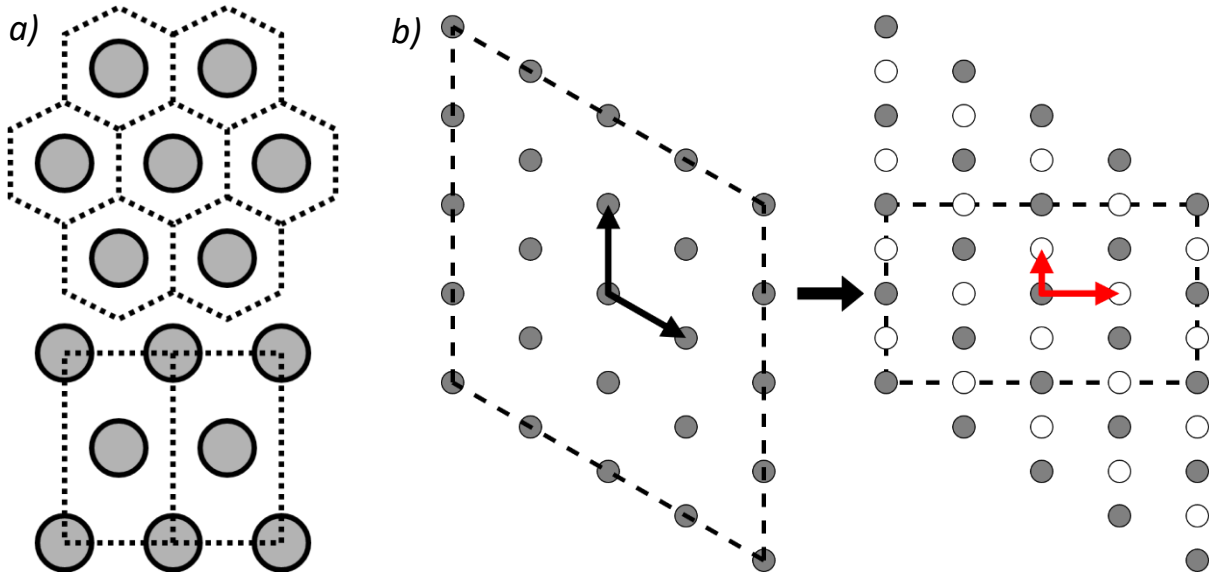


Figure 33: Diagram a) shows how a hexagonal lattice of circles (top), can also be represented as a centred rectangular lattice (bottom). Diagram b) shows how this change of lattice vectors affects the reciprocal lattice vectors. The white points indicate ‘dummy’ points which have Fourier components of zero associated with them. Note the set of non-dummy points included for 5 harmonics is different in the two cases (the dashed black line).

But why go to all this trouble for finding the band structure for a non-primitive crystal unit cell, when the band structure could simply be calculated for the primitive unit cell anyway? The answer is that this method for extracting the band structure of the primitive unit cell from that of the non-primitive unit cell applies to other crystals which do not have a rectangular primitive unit cell, such as centred rectangular crystals, or even higher order non-primitive unit cells.

To demonstrate, a hexagonal crystal can be equivalently represented by a centred rectangular unit cell, as shown in Figure 33. Plugging this unit cell into the calculator, the Fourier series of

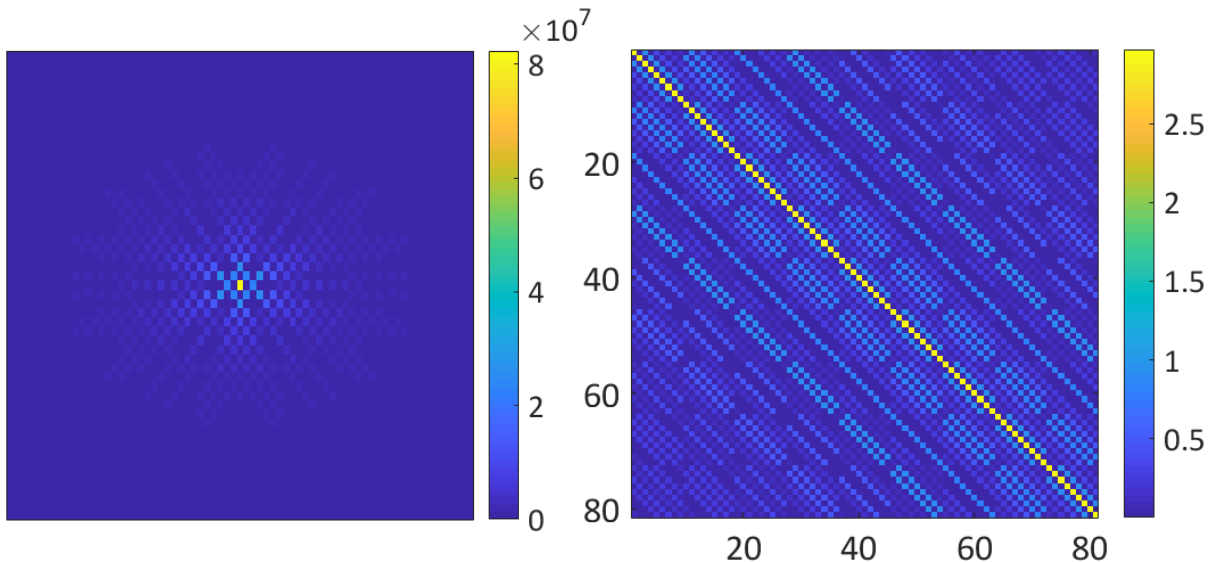


Figure 34: This figure shows the ϵ_r Fourier series for the hexagonal non-primitive cell (left), and its corresponding convolution matrix for 9 harmonics (right). Note the checkerboard pattern in the Fourier series is passed to the convolution matrix.

this non-primitive cell is indeed found to add zeroes to the hexagonal basis Fourier series, giving a checkerboard pattern (see Figure 34).

Using this, the naïve band structure can be filtered to remove non-physical bands, giving the band structure in Figure 35. This has very strong agreement both with the band structure calculated using the HFFT, and with the existing literature. It is important to note though that this method samples a different set of points in reciprocal space to build the band structure – a rectangular instead of rhomboid envelope, as Figure 33 shows. This means that the calculated band structure will be slightly different to that of the HFFT method, especially for small numbers of harmonics where the band structure has not fully converged.

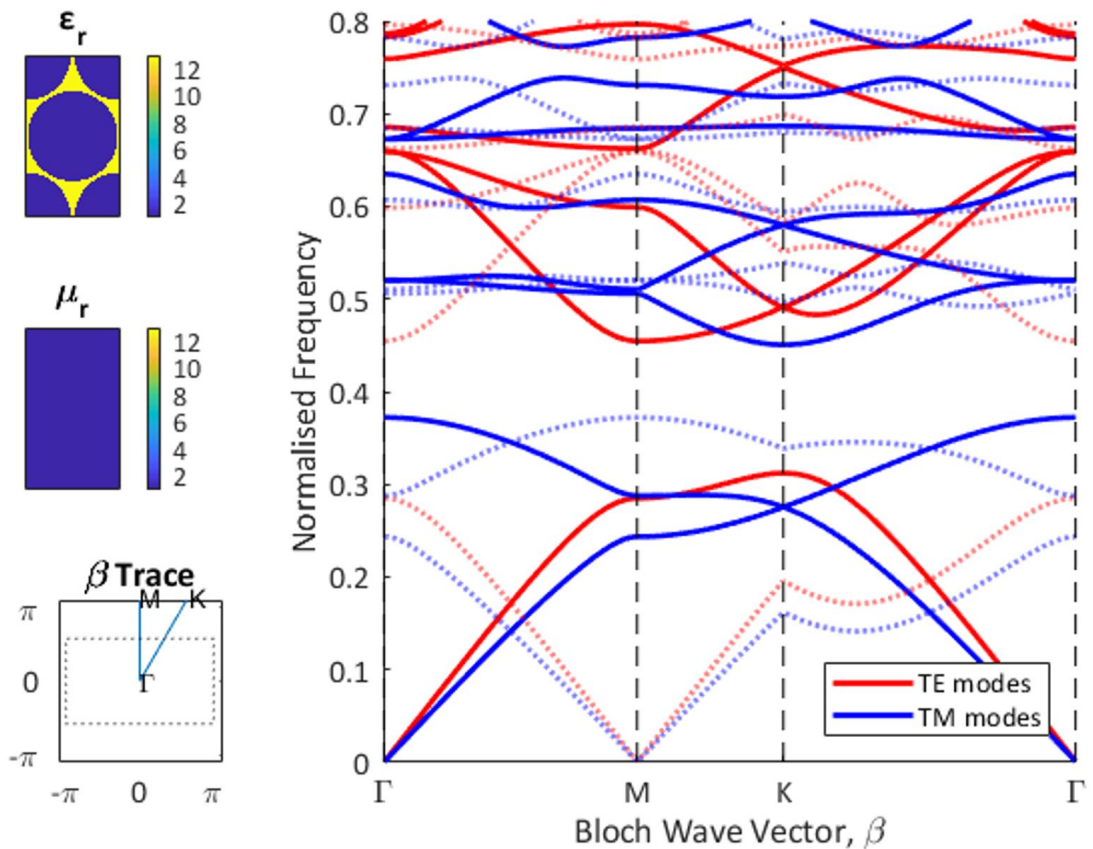


Figure 35: This figure shows calculated band structure for a double hexagonal unit cell, with 21 harmonics, corresponding to the smallest 221 physical harmonics. The non-physical bands are again shown here as semi-transparent and dashed. Note the agreement with Figure 25 and J. Joannopoulos remains very strong when calculated this way [5, p75].

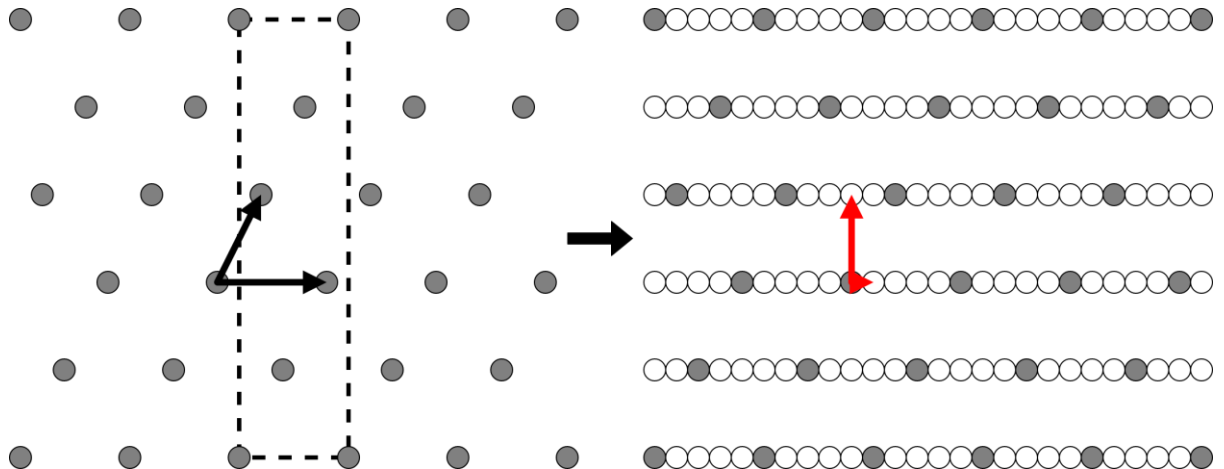


Figure 36: This shows how the Fourier components for an oblique crystal lattice can be found using a rectangular Fourier series. In the left diagram, the grey points show points in reciprocal space which have non-zero Fourier series elements associated with them. The dashed black lines show that 5 primitive unit cells build a rectangular non-primitive unit cell. The black arrows indicate the reciprocal lattice vectors for the Bravais lattice. The right diagram shows the reciprocal lattice vectors for the non-primitive lattice (red arrows) that the FFT of the rectangular unit cell will be associated with. The white points indicate 'dummy' points which have Fourier components of zero. Given an oblique lattice, the positions of the non-dummy points in the FFT are straightforward to calculate.

This extension of the Rumpf method to non-rectangular unit cells does not quite allow for the calculation of the band structure for a general oblique Bravais lattice using the FFT, but it is pretty close. For example, Figure 36 shows how the reciprocal lattice vectors would be changed for a crystal that can be created by tiling rectangular non-primitive unit cells, each containing 5 primitive unit cells. While this would require the FFT to be applied to a unit cell 5 times larger than for an equivalent primitive unit cell, it prevents the need to numerically calculate the Fourier series in a non-rectangular basis for the primitive unit cell. As the name suggests, the Fast Fourier Transform is much faster than calculating the integrals for each Fourier component separately.

8. Conclusions

The primary objective of the project has been completed, with two distinct methods of calculating the band structure of a photonic crystal being explored. Both have been derived from Maxwell's equations and implemented in MATLAB. They have both been shown to converge with increasing numbers of harmonics, and to calculate band structures consistent with the literature for known unit cells, although the Rumpf method appears to give better agreement for non-rectangular lattices. Further, the Rumpf method is able to calculate the band structure for unit cells with periodic magnetic permeability as well, though this was not substantially explored in this report as it is hard to find band structures for such crystals in the literature to verify the calculations.

The Rumpf method has been twice extended, first to utilise the Hexagonal Fast Fourier Transform to calculate the band structure of hexagonal unit cells, and secondly to more

generally extend the method to find the band structures for non-rectangular primitive unit cells which have rectangular non-primitive unit cells. Thus, the method has been extended from being applicable to rectangular Bravais lattices only, to being applicable to rectangular, centred rectangular, hexagonal, and in principle any oblique lattice where $\underline{a}_1 \cdot \underline{a}_2 / a_1$ is rational, as it can then be expressed as a tiling of rectangular non-primitive cells.

This was done by identifying which rows and columns in the eigenproblem matrices corresponded to physically forbidden Fourier components for the Bloch periodic functions, φ_r , and removing these from the matrices before solving them. However, as the number of primitive unit cells in the non-primitive cell increases, the computation and memory cost of this method will rise.

This technique can equally well be implemented in the semi-analytic method, in order to find the Fourier components of non-rectangular unit cells which do not have a simple analytic Fourier series.

In this project the permittivity and permeability of materials in the unit cells were assumed to be isotropic, and non-dispersive. Future work should be done to include these material properties into the calculators to improve their predictions.

9. Acknowledgements

I would like to express my gratitude to my project supervisor, Prof. Martin McCall for his patience and advice during the past year. I also wish to thank Maria del Valle Varo Garcia, Daniel Jones and my project partner for many enlightening and fruitful conversations in relation to this work.

10. Bibliography

- [1] J. W. S. Rayleigh, “On the Influence of Obstacles arranged in Rectangular Order upon the Properties of a Medium”, Philosophical Magazine, Vol. 34, Iss. 211, pp 481-502 (1892). Available from: doi:10.1080/14786449208620364
- [2] E. Yablonovitch, “Inhibited Spontaneous Emission in Solid-State Physics and Electronics”, Physical Review Letters, Vol 58 (1987). Available from: doi:10.1103/PhysRevLett.58.2059
- [3] E. Yablonovitch, T. Gmitter, “Photonic Band Structure: The Face-Centred-Cubic Case”, Physical Review Letters, Vol 63 (1989). Available from: doi:10.1103/PhysRevLett.63.1950
- [4] JH. Park, T. Sudarshan, “Chemical Vapour Deposition”, ASM International (2001). ISBN: 9781615032242
- [5] J. Joannopoulos et al, “Photonic Crystals: Molding the Flow of Light, Second Edition”, Princeton University Press (2011). ISBN: 9781400828241. Available from: <http://ab-initio.mit.edu/book/photonic-crystals-book.pdf>
- [6] US Naval Research Laboratory, Photonic Crystal Fibre SEM Image. Available from: https://www.nrl.navy.mil/nanoscience/sites/edit-www.nrl.navy.mil.nanoscience/files/files/NANO_RESEARCH_IN_OPTICS.pdf

- [7] P. Roberts et al, “Ultimate low loss of hollow-core photonic crystal fibres”, Optics Express, Vol. 13 (2005). Available from: doi:10.1364/OPEX.13.000236
- [8] M. Plihal et all, “Two-dimensional photonic band structures”, Optics Communications, Vol. 80 (1991). Available from: doi:10.1016/0030-4018(91)90250-H
- [9] R. Rumpf, “Lecture 18 -- Maxwell's Equations in Fourier Space” (2017). Available from: <http://emlab.utep.edu/ee5390cem/Lecture%2018%20--%20Maxwell's%20Equations%20in%20Fourier%20Space.pdf>
- [10] R. Rumpf, “Lecture 19 – Plane Wave Expansion Method” (2017). Available from: <http://emlab.utep.edu/ee5390cem/Lecture%2019%20--%20Plane%20Wave%20Expansion%20Method.pdf>
- [11] R. Rumpf, “Lecture 20 -- PWEM Extras” (2017). Available from: <http://emlab.utep.edu/ee5390cem/Lecture%2020%20--%20PWEM%20Extras.pdf>
- [12] J. B. Birdsong and N. I. Rummelt, “The Hexagonal Fast Fourier Transform”, 2016 IEEE International Conference on Image Processing (ICIP), pp 1809-1812 (2016). Available from: doi:10.1109/ICIP.2016.7532670
- [13] Amnon Yariv, Pochi Yeh, “Photonics, Optical Electronics in Modern Communications”, Oxford University Press (2007). ISBN: 9780195179460
- [14] Min Qiu, Sailing He, “Large complete band gap in two-dimensional photonic crystals with elliptic air holes”, Physical Review B, Condensed Matter, Vol. 60 (1999). Available from: doi:10.1103/PhysRevB.60.10610
- [15] J. Yuan et al, “Modeling photonic crystals by boundary integral equations and Dirichlet-to-Neumann maps”, Journal of Computational Physics, Vol. 227 (2008). Available from: doi:10.1016/j.jcp.2008.01.014

Appendices

A) Derivation of Semi-Analytic Non-Magnetic Method Equation

$$\nabla \times \left(\sum_{\underline{\tilde{G}}} K(\underline{\tilde{G}}) e^{i\underline{\tilde{G}} \cdot \underline{r}} \nabla \times \sum_{\underline{G}} (\underline{h}_{\underline{\beta}}(\underline{G}) e^{i\underline{G} \cdot \underline{r}}) e^{i\underline{\beta} \cdot \underline{r}} \right) = k_0^2 \sum_{\underline{G}} (\underline{h}_{\underline{\beta}}(\underline{G}) e^{i\underline{G} \cdot \underline{r}}) e^{i\underline{\beta} \cdot \underline{r}}$$

Starting with Equation (9), the summation terms can be grouped together:

$$\nabla \times \left(\sum_{\underline{\tilde{G}}, \underline{G}} K(\underline{\tilde{G}}) e^{i\underline{\tilde{G}} \cdot \underline{r}} \nabla \times \underline{h}_{\underline{\beta}}(\underline{G}) e^{i\underline{G} \cdot \underline{r}} e^{i\underline{\beta} \cdot \underline{r}} \right) = k_0^2 \sum_{\underline{G}} (\underline{h}_{\underline{\beta}}(\underline{G}) e^{i\underline{G} \cdot \underline{r}}) e^{i\underline{\beta} \cdot \underline{r}}$$

The only spatial dependence in the inner curl is in the exponential functions, and so:

$$\nabla \times \left(\sum_{\underline{G}, \underline{G}} K(\underline{\tilde{G}}) e^{i\underline{\tilde{G}} \cdot \underline{r}} i \left(\underline{G} + \underline{\beta} \right) \times \underline{h}_{\beta}(\underline{G}) e^{i\underline{G} \cdot \underline{r}} e^{i\underline{\beta} \cdot \underline{r}} \right) = k_0^2 \sum_{\underline{G}} \left(\underline{h}_{\beta}(\underline{G}) e^{i\underline{G} \cdot \underline{r}} \right) e^{i\underline{\beta} \cdot \underline{r}}$$

Merging exponential terms and moving the outer curl inside the summation yields:

$$i \sum_{\underline{G}, \underline{G}} K(\underline{\tilde{G}}) \nabla \times \left(\left(\underline{G} + \underline{\beta} \right) \times \underline{h}_{\beta}(\underline{G}) e^{i(\underline{G} + \underline{\tilde{G}} + \underline{\beta}) \cdot \underline{r}} \right) = k_0^2 \sum_{\underline{G}} \underline{h}_{\beta}(\underline{G}) e^{i(\underline{G} + \underline{\beta}) \cdot \underline{r}}$$

Relabelling $\underline{G}' = \underline{\tilde{G}} + \underline{G}$ gives:

$$i \sum_{\underline{G}, \underline{G}'} K(\underline{G}' - \underline{G}) \nabla \times \left(\left(\underline{G} + \underline{\beta} \right) \times \underline{h}_{\beta}(\underline{G}) e^{i(\underline{G}' + \underline{\beta}) \cdot \underline{r}} \right) = k_0^2 \sum_{\underline{G}} \underline{h}_{\beta}(\underline{G}) e^{i(\underline{G} + \underline{\beta}) \cdot \underline{r}}$$

Again, the only spatial components are in the exponential term, so the curl becomes:

$$\begin{aligned} i \sum_{\underline{G}, \underline{G}'} K(\underline{G}' - \underline{G}) i \left(\underline{G}' + \underline{\beta} \right) \times \left(\left(\underline{G} + \underline{\beta} \right) \times \underline{h}_{\beta}(\underline{G}) e^{i(\underline{G}' + \underline{\beta}) \cdot \underline{r}} \right) &= k_0^2 \sum_{\underline{G}} \underline{h}_{\beta}(\underline{G}) e^{i(\underline{G} + \underline{\beta}) \cdot \underline{r}} \\ - \sum_{\underline{G}, \underline{G}'} K(\underline{G}' - \underline{G}) \left(\underline{G}' + \underline{\beta} \right) \times \left(\left(\underline{G} + \underline{\beta} \right) \times \underline{h}_{\beta}(\underline{G}) \right) e^{i(\underline{G}' + \underline{\beta}) \cdot \underline{r}} &= k_0^2 \sum_{\underline{G}} \underline{h}_{\beta}(\underline{G}) e^{i(\underline{G} + \underline{\beta}) \cdot \underline{r}} \end{aligned}$$

Relabelling \underline{G} to \underline{G}' on the RHS, then puts the exponential term in the same form as the LHS, forcing each \underline{G}' term in the summations to match on both sides:

$$\begin{aligned} - \sum_{\underline{G}, \underline{G}'} K(\underline{G}' - \underline{G}) \left(\underline{G}' + \underline{\beta} \right) \times \left(\left(\underline{G} + \underline{\beta} \right) \times \underline{h}_{\beta}(\underline{G}) \right) e^{i(\underline{G}' + \underline{\beta}) \cdot \underline{r}} &= k_0^2 \sum_{\underline{G}'} \underline{h}_{\beta}(\underline{G}') e^{i(\underline{G}' + \underline{\beta}) \cdot \underline{r}} \\ - \sum_{\underline{G}} K(\underline{G}' - \underline{G}) \left(\underline{G}' + \underline{\beta} \right) \times \left(\left(\underline{G} + \underline{\beta} \right) \times \underline{h}_{\beta}(\underline{G}) \right) &= k_0^2 \underline{h}_{\beta}(\underline{G}') \end{aligned}$$

As stated in Equation (10).

B) Derivation of 1D Box Function Fourier Series

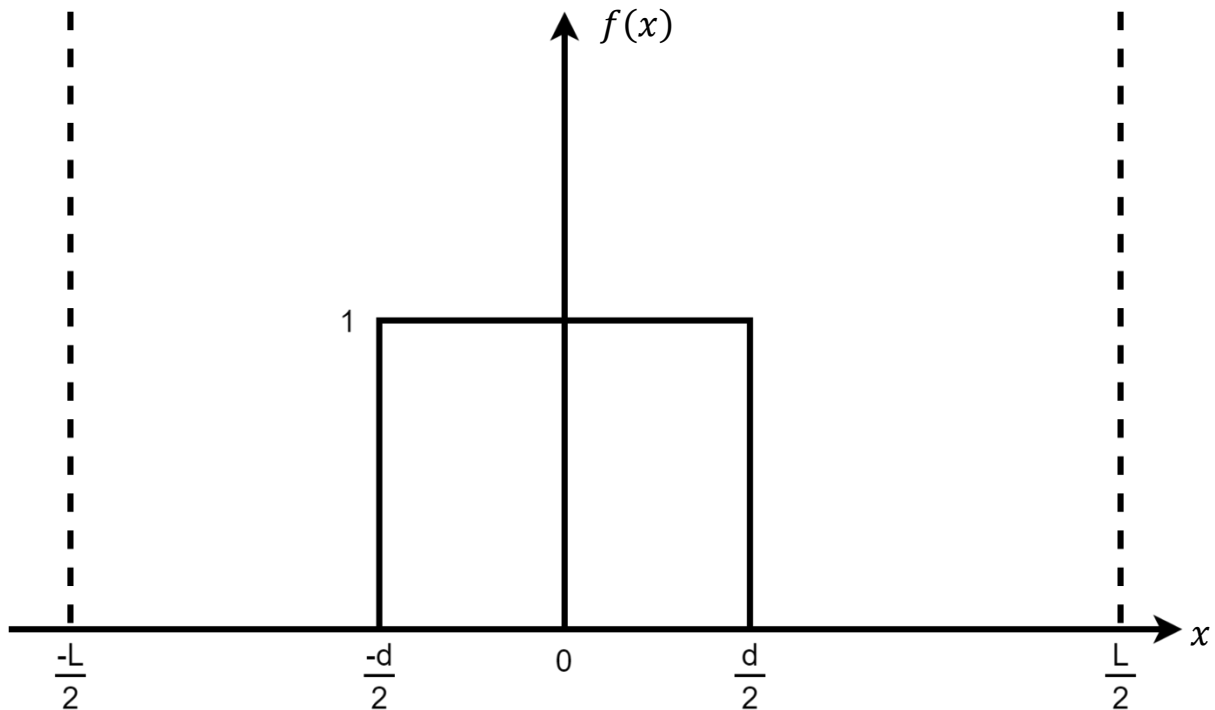


Figure B1: This diagram shows the 1D box function of width d within a unit cell of width L .

The 1D box function, $f(x)$ (see Figure B1), can be expanded using the complex Fourier series:

$$f(x) = \sum_{n=-\infty}^{\infty} A_n e^{\frac{2\pi i n x}{L}}$$

$$A_n = \frac{1}{L} \int_{-\frac{L}{2}}^{\frac{L}{2}} f(x) e^{-\frac{2\pi i n x}{L}} dx$$

But in the case of a box function:

$$f(x) = \begin{cases} 1, & -\frac{d}{2} < x < \frac{d}{2} \\ 0, & \text{otherwise} \end{cases}$$

Thus the $n = 0$ term is:

$$A_0 = \frac{1}{L} \int_{-\frac{L}{2}}^{\frac{L}{2}} f(x) e^0 dx = \frac{1}{L} \int_{-\frac{d}{2}}^{\frac{d}{2}} dx$$

$$A_0 = \frac{d}{L}$$

Which is the average value over the unit cell, as expected. For the $n \neq 0$ terms:

$$\begin{aligned}
A_n &= \frac{1}{L} \int_{-\frac{L}{2}}^{\frac{L}{2}} f(x) e^{\frac{-2\pi i n x}{L}} dx \\
A_n &= \frac{1}{L} \int_{-\frac{d}{2}}^{\frac{d}{2}} e^{\frac{-2\pi i n x}{L}} dx = \frac{1}{L} \left[\frac{-L}{2\pi i n} e^{\frac{-2\pi i n x}{L}} \right]_{-\frac{d}{2}}^{\frac{d}{2}} \\
A_n &= \frac{-1}{n\pi} \frac{1}{2i} \left(e^{\frac{-in\pi d}{L}} - e^{\frac{in\pi d}{L}} \right) = \frac{1}{n\pi} \sin \frac{n\pi d}{L} \\
A_n &= \frac{d}{L} \operatorname{sinc} \frac{n\pi d}{L}
\end{aligned}$$

i.e. the components of the complex Fourier series of a box function are given by the sinc function. By multiplying every term in the series by some constant, and by adding some value to the entire cell (changing the A_0 term), a box function between two arbitrary values can be obtained.

C) Derivation of 2D Circular Rod Fourier Series

In principle it is necessary to specify the Bravais lattice for the unit cell before the Fourier series can be calculated, but in the case of a circular feature it is not strictly necessary. Consider a unit cell of area a_{cell} which has a permittivity value of ϵ_a inside a circle of radius r_a , and a value of ϵ_b outside that radius. This can be expressed as a Fourier series:

$$\epsilon(\underline{r}) = \sum_{\underline{G}} A_{\underline{G}} e^{i\underline{G} \cdot \underline{r}},$$

where:

$$A_{\underline{G}} = \frac{1}{a_{cell}} \iint_{Cell} \epsilon(\underline{r}) e^{-i\underline{G} \cdot \underline{r}} d^2 \underline{r}$$

But $\epsilon(\underline{r})$ can also be expressed as:

$$\epsilon(\underline{r}) = \epsilon_b + (\epsilon_a - \epsilon_b) S(r),$$

where:

$$S(r) = \begin{cases} 1, & r \leq r_a \\ 0, & \text{otherwise} \end{cases}$$

Thus:

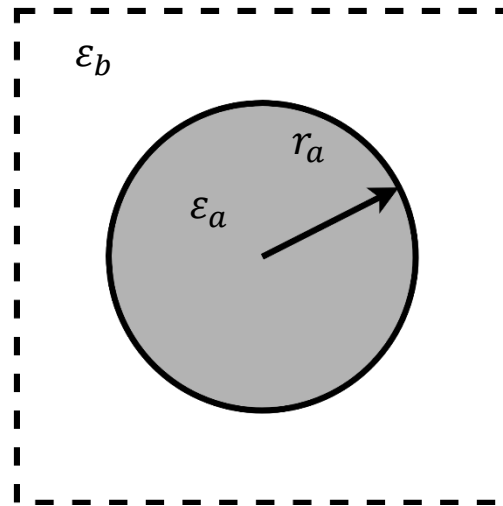


Figure C1: This image shows the general 2D unit cell for a circular rod of $\epsilon_r = \epsilon_a$ and radius r_a in a surrounding material with $\epsilon_r = \epsilon_b$.

$$A_{\underline{G}} = \frac{1}{a_{cell}} \iint_{Cell} (\varepsilon_b + (\varepsilon_a - \varepsilon_b)S(r)) e^{-i\underline{G}\cdot \underline{r}} d^2 \underline{r}$$

$$A_{\underline{G}} = \frac{1}{a_{cell}} \left(\iint_{Cell} \varepsilon_b e^{-i\underline{G}\cdot \underline{r}} d^2 \underline{r} + \int_0^{2\pi} \int_0^{r_a} (\varepsilon_a - \varepsilon_b) r e^{-i\underline{G}\cdot \underline{r}} dr d\varphi \right)$$

For the first integral, it will be 0 if \underline{G} is anything other than 0. For the second integral, expanding out the dot product gives:

$$A_{\underline{G}} = \varepsilon_b \delta(\underline{G}) + \frac{\varepsilon_a - \varepsilon_b}{a_{cell}} \int_0^{2\pi} \int_0^{r_a} e^{-iGr \cos \varphi} dr d\varphi$$

But:

$$e^{-iGr \cos \varphi} = e^{-iGr \sin(\varphi - \frac{\pi}{2})} = \sum_{m=-\infty}^{\infty} r J_m(Gr) e^{im(\varphi - \frac{\pi}{2})}$$

But for all $l \neq 0$, the integral over φ will go to zero. Therefore:

$$A_{\underline{G}} = \varepsilon_b \delta(\underline{G}) + \frac{2\pi(\varepsilon_a - \varepsilon_b)}{a_{cell}} \int_0^{r_a} r J_0(Gr) dr$$

Using:

$$\int_0^u u' J_0(u') = u J_1(u),$$

$$A_{\underline{G}} = \varepsilon_b \delta(\underline{G}) + \frac{2\pi(\varepsilon_a - \varepsilon_b)}{a_{cell}} \frac{r_a}{G} J_1(Gr_a)$$

Then using the fill fraction of the unit cell, $f = \frac{\pi r_a^2}{a_{cell}}$:

$$A_{\underline{G}} = \varepsilon_b \delta(\underline{G}) + 2f(\varepsilon_a - \varepsilon_b) \frac{J_1(Gr_a)}{Gr_a}$$

D) Hexagonal Fast Fourier Transform (HFFT)

The algorithm for the HFFT is best described by its authors J. Birdsong and N. Rummelt [12], and effectively assumes the unit cells are offset rectangles as shown in Figure D1. However, to apply the HFFT to a unit cell, the unit cell must first be expressed in a hexagonal basis, as opposed to the rectangular basis of an array. This is done using the ‘Array Set Addressing’ (ASA) coordinate system. The unit cell is sampled in a triangular pattern, and the results stored in two rectangular arrays, as in Figure D2.

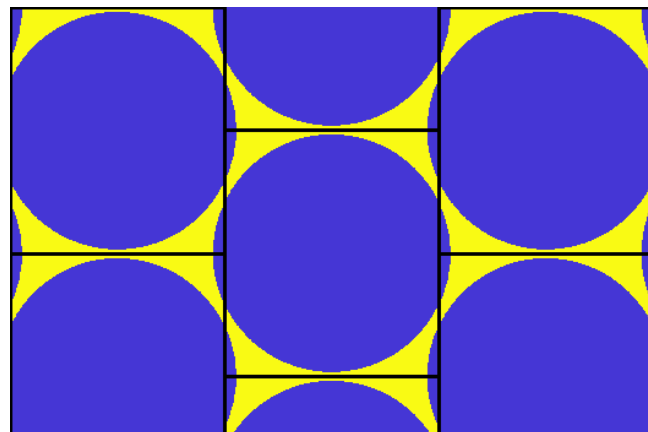


Figure D1: This image shows how a unit cell defined under the ASA coordinate system tessellates over all space. Each column is offset by half a cell height from its neighbours to create a hexagonal tessellation pattern.

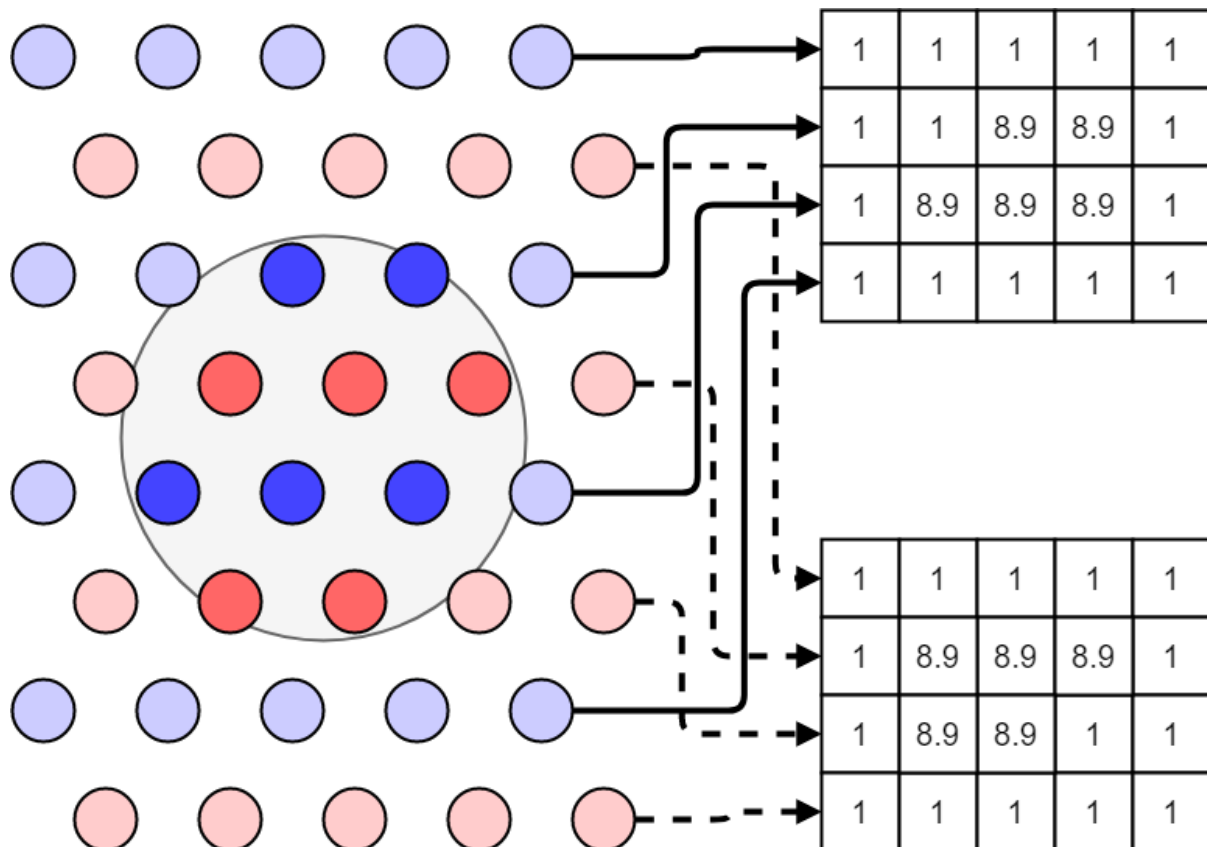


Figure D2: This image shows how a unit cell is sampled by the triangular grid of points, and how the points are allocated to each component array. Points within the grey circle have a value of 8.9, and those outside have a value of 1, like the unit cells in Figures 11 and 17. In practice, the grid of points used to calculate the HFFT will have at least 1 million points

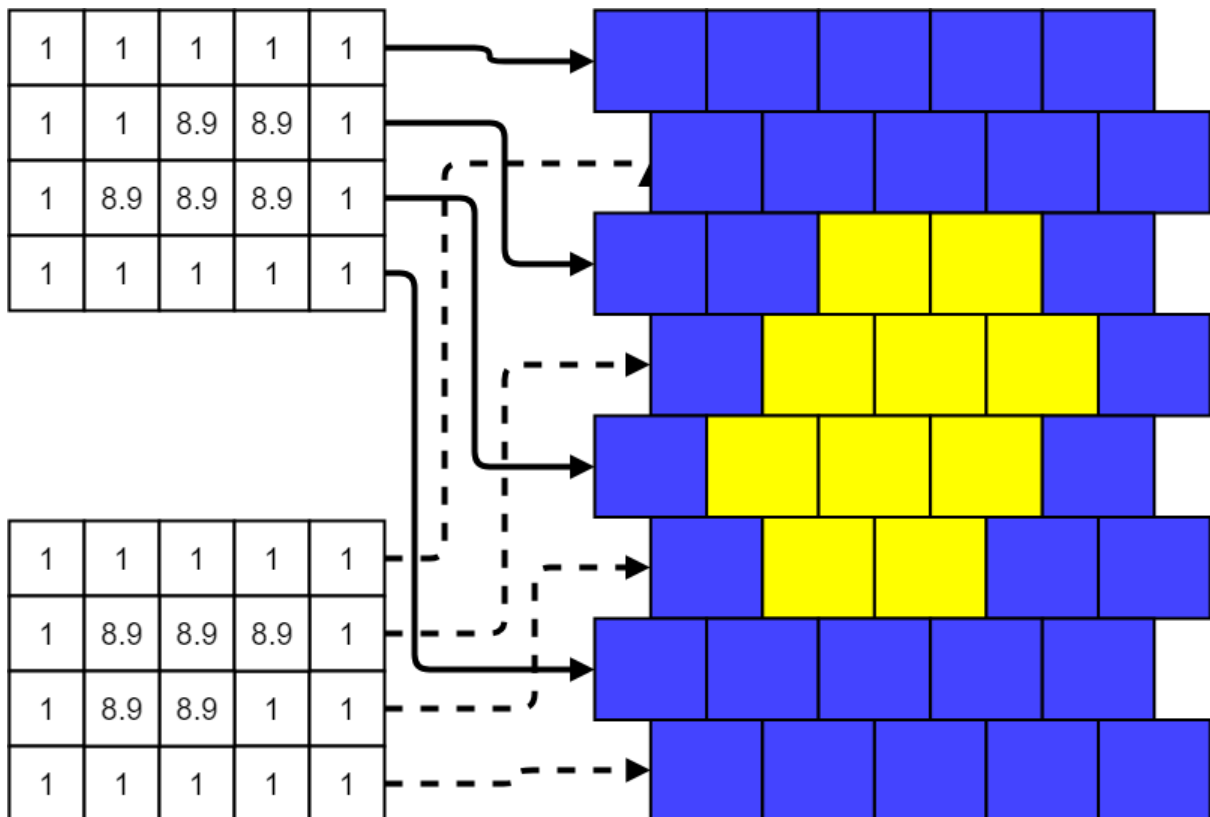


Figure D3: This image shows how a unit cell defined using ASA coordinates can be redrawn over a rectangular array such as in a standard image file. Each point in the ASA coordinates maps to at least two points in the rectangular array. This allows the offset property of the two component arrays to be preserved

To draw a unit cell defined in ASA coordinates, as in Figures 25 and D1, each point is given two pixels on a rectangular array, as shown in Figure D3.